MAY 13 1998
0830-L-02
NAS 1.29/3-2:98-05

NASA TechBriefs

National Aeronautics and
Space Administration

Electronic Components and Circuits

Electronic Systems

Physical Sciences

Materials

Computer Programs

Mechanics

Machinery

Fabrication Technology

Mathematics and Information Sciences

Life Sciences

COMPLETED

98-05

May 1998

CA 99008843

INTRODUCTION

Tech Briefs are short announcements of new technology derived from the research and development activities of the National Aeronautics and Space Administration. These Briefs emphasize information considered likely to be transferable across industrial, regional, or disciplinary lines and are issued to encourage commercial application.

Availability of NASA Tech Briefs and TSP's

Distribution of NASA Tech Briefs, a monthly periodical publication, is limited to engineers in U.S. Industry and to other domestic technology transfer agents. Requests for individual Tech Briefs or for Technical Support Packages (TSP's) announced herein should be addressed to

NASA Center for AeroSpace Information
Technology Transfer Office
800 Elkridge Landing Rd.
Linthicum Heights, MD 21090-2934
Telephone No. (301) 621-0245

Please reference the three-letter, five-digit control number located at the end of each Tech Brief. Information on NASA's Technology Utilization Program, its documents, and services is also available at the same facility.

Technology Utilization Officers and Patent Counsels are located at NASA field installations to provide technology-transfer access to industrial users. Inquiries can be made by writing to NASA field installations listed below.

Technology Utilization Officers and Patent Counsels

Ames Research Center
Technology Utilization Officer
Mail Code 223-3
Moffett Field, CA 94035

Patent Counsel
Mail Code 200-11
Moffett Field, CA 94035

Goddard Space Flight Center
Technology Utilization Officer
Mail Code 702-1
Greenbelt, MD 20771

Patent Counsel
Mail Code 204
Greenbelt, MD 20771

Lyndon B. Johnson Space Center
Technology Utilization Officer
Mail Code IC-4
Houston, TX 77058

Patent Counsel
Mail Code AL3
Houston, TX 77058

John F. Kennedy Space Center
Technology Utilization Officer
Mail Stop PT-PMO-A
Kennedy Space Center, FL 32899

Patent Counsel
Mail Code PT-PAT
Kennedy Space Center, FL 32899

Langley Research Center
Technology Utilization Officer
Mail Stop 143
Hampton, VA 23665

Patent Counsel
Mail Code 279
Hampton, VA 23665

Lewis Research Center
Technology Utilization Officer
Mail Stop 7-3
21000 Brookpark Road
Cleveland, OH 44135

Patent Counsel
Mail Code LE-LAW
21000 Brookpark Road
Cleveland, OH 44135

Jet Propulsion Laboratory
Technology Utilization Officer
Mail Stop 156-211
4800 Oak Grove Drive
Pasadena, CA 91109

NASA Resident Office-JPL
Technology Utilization Officer
Mail Stop 180-801
4800 Oak Grove Drive
Pasadena, CA 91109

Patent Counsel
Mail Code 180-801
4800 Oak Grove Drive
Pasadena, CA 91109

George C. Marshall Space Flight Center
Technology Utilization Officer
Code AT01
Marshall Space Flight Center, AL 35812

Patent Counsel
Mail Code CC01
Marshall Space Flight Center, AL 35812

John C. Stennis Space Center
Technology Utilization Officer
Code HA-30
Stennis Space Center, MS 39529

NASA Headquarters
Technology Utilization Officer
Code CU
Washington, DC 20546

Assistant General Counsel for Patent Matters
Code GP
Washington, DC 20546

Dryden Flight Research Center
Technology Utilization Officer
M/S D21-31
Bldg. 4832 Whse 7
Lilly Dr.
Edwards, CA 93523

BLANK PAGE

NASA TechBriefs

National Aeronautics and
Space Administration

May 1998
98-05

5 Electronic Components and Circuits

11 Electronic Systems

17 Physical Sciences

23 Materials

33 Computer Programs

37 Mechanics

43 Machinery

47 Fabrication Technology

This document was prepared under the sponsorship of the National Aeronautics and Space Administration. Neither the United States Government nor any person acting on behalf of the United States Government assumes any liability resulting from the use of the information contained in this document, or warrants that such use will be free from privately owned rights.

BLANK PAGE

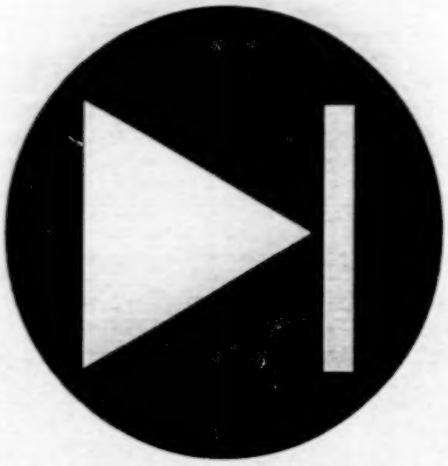

Electronic Components and Circuits

Hardware, Techniques, and Processes

7 Bounceless Switch/Monostable Multivibrator
7 Exploiting Brillouin Scattering in Analog Signal Processing
8 More Uses for Brillouin Amplification
9 Optoelectronic Oscillators Based on Brillouin Scattering

Books and Reports

10 Overview of Tapered-Slot Antennas

BLANK PAGE

Bounceless Switch/Monostable Multivibrator

Monostable circuit debounces a switch while allowing for the monostable circuit to be activated by an electronic circuit.

Marshall Space Flight Center, Alabama

A circuit has been designed to debounce a mechanical switch, which is used to activate a digital circuit. Contacts tend to make and break connections several times until the switch contacts settle out. The repetitive activity plays havoc with digital circuits because more than one state condition could be activated by the switch as it bounces around between state conditions.

The switch debouncer circuit will recognize the first state condition activated by the switch and latch the circuit into this condition for a predetermined period of time until the switch bouncing settles down. In this way, the circuit will respond to only one pulse generation performed by the depressing of the switch and not several state transitions caused by contact bouncing.

This circuit can also be used for a monostable multivibrator or one-shot multivibrator. A monostable multivibrator generates a single pulse output when activated by a trigger command. The pulse width or pulse duration in this circuit is defined by selecting the proper values of a resistor and capacitor arrangement.

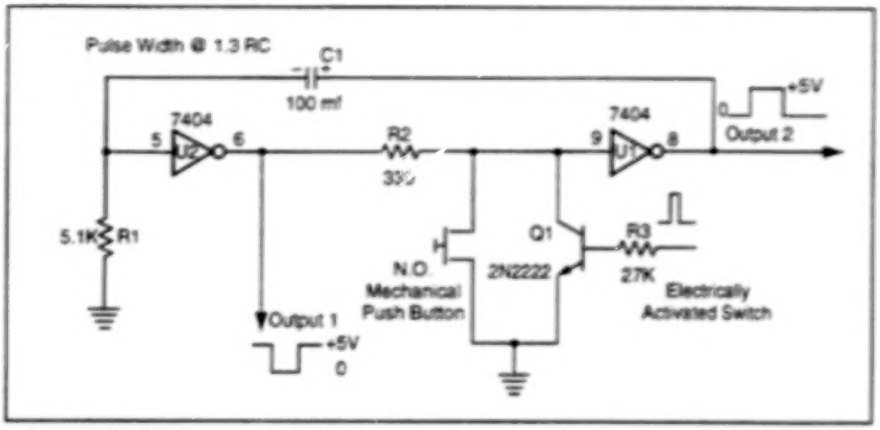

A Monostable Multivibrator generates a single pulse output when activated by a trigger command.

This work was done by Randal S. McNichol of the **Marshall Space Flight Center**. *Further information is contained in a TSP [see page 1].*

MFS-31141

Exploiting Brillouin Scattering in Analog Signal Processing

Heretofore a nuisance, this phenomenon can be used for amplification and frequency conversion.

NASA's Jet Propulsion Laboratory, Pasadena, California

Stimulated Brillouin scattering (SBS) in optical fibers can be exploited to obtain frequency conversion with amplification and frequency-selective amplification in photonic signal-transmission and signal-processing systems. SBS has been found to be particularly useful in photonic systems that handle optical carrier signals modulated with relatively narrow-band radio-frequency (RF) signals that are typically of analog origin.

Brillouin scattering is the scattering of photons by phonons. It can occur spontaneously at low optical power levels and can be stimulated by narrow-band optical signals above threshold power levels that can be as low as a few milliwatts in some optical fibers. Because the threshold power for SBS in an optical fiber is proportional to the spectral width of the input optical signal, SBS does little harm in digital communication systems, in which bandwidths are typically large and power levels of the order of microwatts usually suffice to achieve adequate signal-to-noise ratios. However, in analog communication systems, spectral widths are smaller and power levels of the order of milliwatts are usually needed, so that SBS becomes an issue.

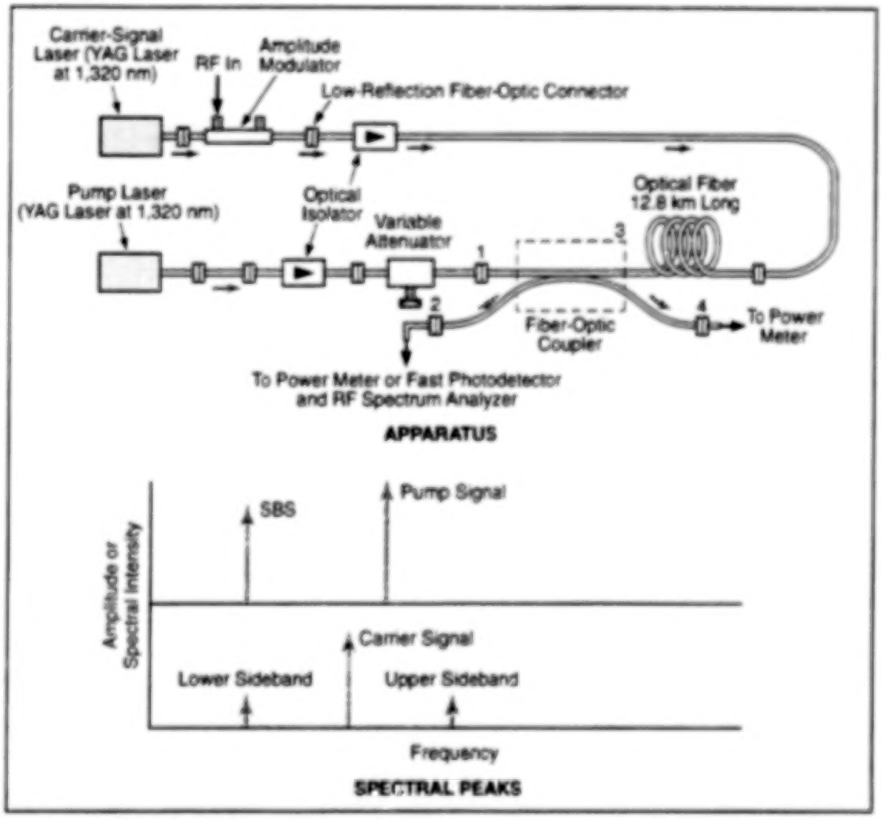

The Lower Sideband of the optical carrier signal as modulated by the RF signal is made to coincide in frequency with the SBS peak. As a result, the lower sideband is amplified by SBS.

SBS is the most sensitive nonlinear optical effect in optical fibers. At a signal power level above the threshold in a given fiber, SBS generates an acoustic grating via the electrostrictive effect, and the grating gives rise to back-scattering of the forward-propagating optical signal. The back-scattering limits the forward-propagating optical power that can be delivered to the output end of the fiber; in other words, the net effect is one of throughput saturation. Thus, heretofore, SBS has been regarded as a nuisance in narrow-band photonic/RF communication systems.

Experiments have shown that when a single-frequency optical signal is launched into an optical fiber, SBS typically occurs with a spectral peak at frequency of the order of a few gigahertz below the signal frequency, and the 6-dB width of the SBS spectrum is typically of the order of 10 MHz. The experiments have also shown that for a given fiber, the SBS peak frequency and spectral width are independent of the signal power. These findings point the way to the use of a single-frequency optical signal as a pump signal in a scheme to achieve frequency-selective amplification, as described next.

The upper part of the figure schematically illustrates a laboratory SBS amplification apparatus, while the lower part of the figure depicts the spectral peaks present during operation. A pump signal is generated by an yttrium/aluminum/garnet (YAG) laser at a wavelength of 1,320 nm and coupled into one end of a 12.8-km-long optical fiber. Another YAG laser generates a carrier signal; this signal is amplitude-modulated with an RF signal (by use of a $LiNbO_3$ Mach-Zehnder Modulator) and coupled into the other end of the long optical fiber. The apparatus is designed to minimize reflections. The back-scattered optical power is sampled via port 2 of a four-port fiber-optic coupler, while the input (forward-propagating) pump power is sampled via port 4 of the coupler.

The pump or the carrier laser is adjusted so that the frequency of the carrier signal is lower than that of the pump signal by such an amount as to place the lower sideband of the modulated signal at the SBS peak. As a result, the lower sideband joins the back-scattered signal and becomes amplified by the nonlinear SBS effect. The amount of amplification diminishes gradually with departure of frequency from the SBS peak. The carrier and lower sideband are sufficiently distant in frequency from the SBS peak that they are not amplified.

Frequency conversion with amplification can be effected by an apparatus that is similar except that the modulator includes two independent RF input ports with a high degree of mutual isolation. RF modulation is coupled in through one port, while a local-oscillator (LO) signal is coupled in through the other port. The pump and carrier frequencies are adjusted to place the lower LO sideband at the SBS frequency so that the LO signal becomes amplified. The amplified LO signal is then mixed with the RF sidebands to obtain stronger up- and down-converted signals. Optionally, one could choose the frequencies to amplify the lower RF modulation sideband instead of the lower LO sideband, but in that case, the RF-amplification bandwidth would be limited by the SBS bandwidth.

This work was done by Xiaotian Steve Yao of Caltech for **NASA's Jet Propulsion Laboratory**. *Further information is contained in a TSP [see page 1].*

In accordance with Public Law 96-517, the contractor has elected to retain title to this invention. Inquiries concerning rights for its commercial use should be addressed to

Technology Reporting Office
JPL
Mail Stop 122-116
4800 Oak Grove Drive
Pasadena, CA 91109
(818) 354-2240

Refer to NPO-20091, volume and number of this NASA Tech Briefs *issue, and the page number.*

More Uses for Brillouin Amplification

Phase modulation can be converted to amplitude modulation.

NASA's Jet Propulsion Laboratory, Pasadena, California

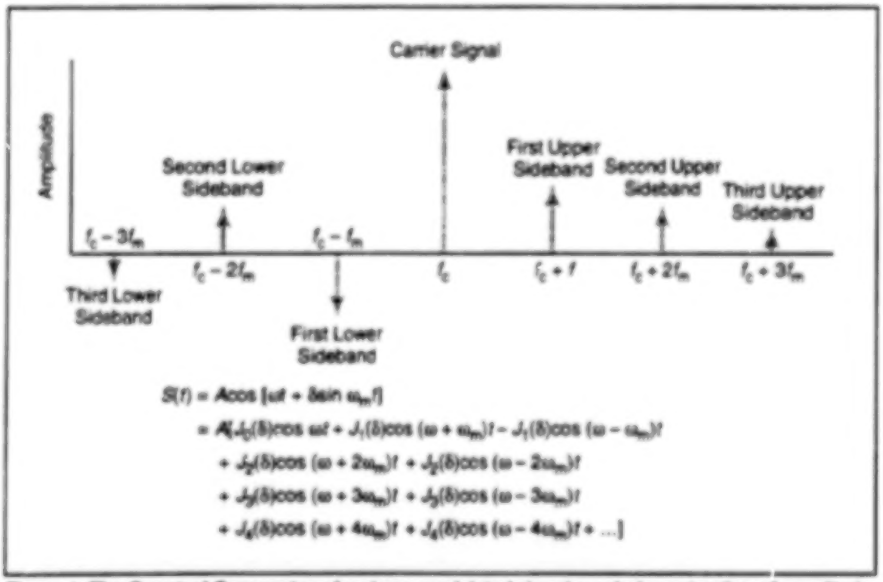
Carrier Signal
Amplitude
Second Lower Sideband
First Upper Sideband
Second Upper Sideband
Third Upper Sideband
$f_c - 3f_m$
$f_c - 2f_m$
$f_c - f_m$
f_c
$f_c + f$
$f_c + 2f_m$
$f_c + 3f_m$
Third Lower Sideband
First Lower Sideband
$S(t) = A\cos[\omega t + \delta\sin\omega_m t]$
$= A[J_0(\delta)\cos\omega t + J_1(\delta)\cos(\omega + \omega_m)t - J_1(\delta)\cos(\omega - \omega_m)t$
$+ J_2(\delta)\cos(\omega + 2\omega_m)t + J_2(\delta)\cos(\omega - 2\omega_m)t$
$+ J_3(\delta)\cos(\omega + 3\omega_m)t + J_3(\delta)\cos(\omega - 3\omega_m)t$
$+ J_4(\delta)\cos(\omega + 4\omega_m)t + J_4(\delta)\cos(\omega - 4\omega_m)t + \ldots]$

Figure 1. The Spectral Symmetry of a phase-modulated signal precludes extraction of amplitude modulation via beat notes and simple detection. Here S is the instantaneous signal amplitude, t is time, $\omega = 2\pi f_c$ where f_c is the carrier frequency, $\omega_m = 2\pi f_m$, δ is the maximum phase deviation, and J_i (i an integer) denotes a Bessel function.

Some additional applications have been proposed to exploit amplification by stimulated Brillouin scattering ("Brillouin Amplification" for short), building on the concepts introduced in the preceding article. Chief among the proposed applications is conversion of a phase-modulated optical signal to an amplitude-modulated optical or electrical signal with stability greater than that previously achievable, and without need for bias.

The difficulty of converting a phase-modulated optical signal to an amplitude-modulated optical or electrical signal arises from the essential nature of any phase-modulated signal. As illustrated in Figure 1, a phase-modulated signal includes many pairs of sidebands at integer multiples of the modulation frequency, f_m, above and below the carrier frequency. For each upper sideband, there is a corresponding lower sideband of equal magnitude, and the difference between the phases of the upper sideband and the carrier is the opposite of the differ-

ence between the phases of the lower sideband and the carrier. One cannot obtain amplitude modulation through the mere detection of the phase-modulated signal because the symmetry between the upper and lower sidebands gives rise to a corresponding symmetry in the beat notes among all the sidebands and between the sidebands and the carrier.

The chief proposal for converting phase modulation to amplitude modulation involves the use of frequency-selective amplification of one of the lower sidebands to break the symmetry between this sideband and its corresponding upper sideband. Brillouin amplification offers the frequency selectivity needed for this purpose. For example, as illustrated in Figure 2, one could adjust the pump and carrier frequencies to place the first lower sideband at the Brillouin-scattering spectral peak. This adjustment would cause the first lower sideband (but not the carrier or the first upper sideband) to become Brillouin-amplified, as described in the preceding article. The beat between the carrier and the preferentially amplified first lower sideband would constitute the major part of the amplitude-modulated output signal. The amplitude modulation would be extremely stable in that it would be immune to fluctuations in the carrier frequency, the temperature, and the length of the optical fiber. In addition, the Brillouin amplification of the chosen sideband would make this technique the most efficient of all techniques for phase-to-amplitude conversion.

Other proposed applications of Brillouin amplification for conversion from phase to amplitude modulation include photonic frequency conversion, photonic frequency multiplexing, photonic generation of harmonics, and photonic amplification and shaping of optical pulses. The pulse application would be the most complex because it would involve the use of multiple pump lasers to achieve Brillouin amplification at multiple selected sidebands of a phase-modulated signal or at multiple modes of a mode-locked laser.

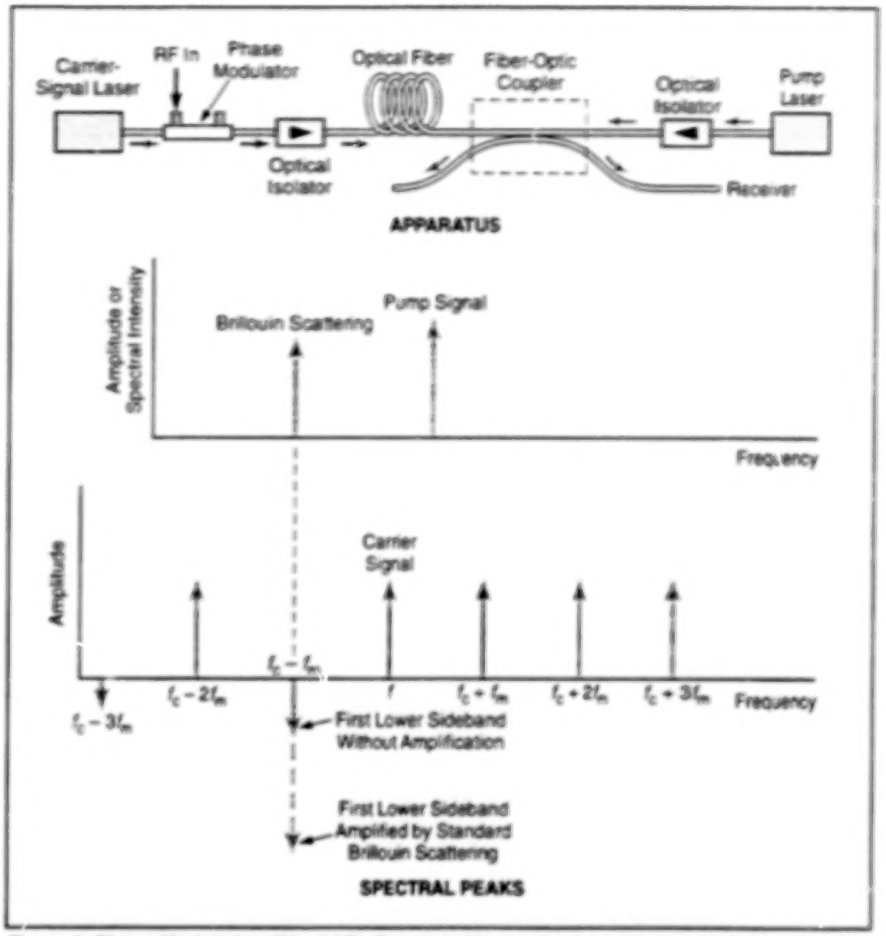

Figure 2. **Phase Modulation Would Be Converted** to amplitude modulation as follows: The first lower sideband of the phase-modulated signal would be Brillouin-amplified, then detected to obtain amplitude modulation in the form of the beat note between the carrier and the first lower sideband.

This work was done by Xiaotian Steve Yao of Caltech for **NASA's Jet Propulsion Laboratory**. *Further information is contained in a TSP [see page 1].*

In accordance with Public Law 96-517, the contractor has elected to retain title to this invention. Inquiries concerning rights for its commercial use should be addressed to

Technology Reporting Office
JPL
Mail Stop 122-116
4800 Oak Grove Drive
Pasadena, CA 91109
(818) 354-2240

Refer to NPO-20092, volume and number of this NASA Tech Briefs *issue, and the page number.*

Optoelectronic Oscillators Based on Brillouin Scattering

Electronic amplifiers and filters are not needed.

NASA's Jet Propulsion Laboratory, Pasadena, California

An improved type of optoelectronic oscillator is based on Brillouin amplification. An oscillator of this type converts light energy into an electro-optical oscillation, typically at a frequency of several gigahertz. It offers several advantages over other electro-optical and over all-electronic oscillators:

- There is no need for a relatively bulky, expensive, power-consuming electronic microwave amplifier.
- Without the flicker noise associated with an electronic microwave amplifier, it should be possible to obtain lower oscillator phase noise.
- The narrow gain bandwidth of Brillouin amplification provides band-pass filtering, making it unnecessary to use a relatively bulky electrical band-pass filter; this feature contributes potential for miniaturization and integration.
- The frequency of oscillation can be tuned over a broad range by changing the frequency of one or two pump laser(s).
- A phase modulator can be used in place of a more-expensive and higher-loss amplitude modulator. Because no bias is necessary for a phase modulator, the bias drift associated with an amplitude modulator is eliminated.

The device is based on Brillouin selective sideband amplification (BSSA), the basic principles of which were described in "Exploiting Brillouin Scattering in Analog Signal Processing" (NPO-20091) and "More Uses for Brillouin Amplification" (NPO-20092), pages 7 and 8. To recapitulate: Brillouin scattering is the scattering of photons by phonons and is the most sensitive nonlinear optical effect in optical

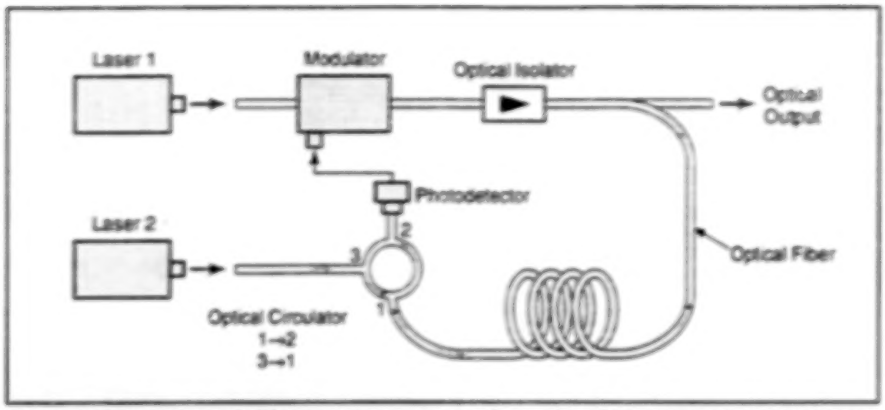

This **Simplified Schematic Diagram** represents one of a number of developmental optoelectronic oscillators based on Brillouin amplification.

fibers. At a laser-signal power level above a threshold specific to a given optical fiber, SBS generates an acoustic grating via the electrostrictive effect, and the grating gives rise to back-scattering of the forward-propagating optical signal.

Suppose that one laser beam, regarded as a pump signal, is coupled into one end of a long optical fiber. Suppose that another, weaker laser beam, regarded as a carrier signal, is modulated with a radio-frequency signal and coupled into the other end of the long optical fiber. Suppose, further, that the pump or the carrier laser is adjusted so that the carrier frequency is lower than the pump frequency by such an amount as to place the lower sideband of the modulated carrier signal at the SBS peak of the pump signal. As a result, the lower sideband joins the back-scattered pump signal and becomes amplified by the nonlinear SBS effect. The amount of amplification diminishes gradually with departure of the lower sideband frequency from the SBS peak. The carrier and upper sideband are sufficiently distant in frequency from the SBS peak that they are not amplified.

The figure illustrates a basic oscillator of the present type, which exploits Brillouin amplification in an optoelectronic feedback loop. Continuous-wave laser 1 is the carrier laser. The carrier laser beam, at frequency ν_1, passes through an electro-optical modulator and an optical isolator into one end of a long optical fiber that serves as a delay line and as the amplifying medium. Continuous-wave laser 2 is the pump laser. The pump laser beam, at frequency ν_2, is introduced through an optical circulator or optical coupler at the other end of the optical fiber. At the end where the pump beam is introduced, a photodetector detects the modulated carrier beam that has propagated along the fiber to this end. The electrical output of the photodetector is applied to the modulator.

Initially, the signal applied to the modulator consists of noise, and thus the carrier signal is modulated initially by noise. However, the only part of the optical signal spectrum that becomes amplified is the component at the Brillouin-scattering frequency; this component gives rise to a beat signal in the photodetector output. The beat signal then drives the modulator to produce a stronger sideband at the beat frequency below the carrier frequency. Thus, through positive feedback, the beat signal (which constitutes the desired oscillation) becomes stronger until the gain saturates. The frequency of oscillation is given by

$$f_{osc} = \nu_1 - \nu_2 + \nu_{BS},$$

where ν_{BS} is the Stokes frequency shift of Brillouin scattering.

A prototype oscillator was constructed, using an optical fiber 12.8 km long with a Stokes frequency shift of 12.8 GHz at a laser wavelength of 1,320 nm. The beam from a single yttrium aluminum garnet (YAG) laser with an output power of 70 mW was split to generate both the pump and carrier signals at this wavelength ($\nu_1 = \nu_2$ in this case). This apparatus was found to generate an electro-optical oscillation with a power of about −11 dBm at the output of the photodetector. Because the Brillouin gain bandwidth was 10 MHz but the mode spacing associated with the 12.8-km fiber length was <10 kHz, mode hopping was observed. Further development effort would be necessary to eliminate mode hopping.

This work was done by X. Steve Yao of Caltech for **NASA's Jet Propulsion Laboratory**. *Further information is contained in a TSP [see page 1].*

In accordance with Public Law 96-517, the contractor has elected to retain title to this invention. Inquiries concerning rights for its commercial use should be addressed to

Technology Reporting Office
JPL
Mail Stop 122-116
4800 Oak Grove Drive
Pasadena, CA 91109
(818) 354-2240

Refer to NPO-20097, volume and number of this NASA Tech Briefs issue, and the page number.

Books and Reports

Overview of Tapered-Slot Antennas

A document presents a comprehensive overview of the technology of tapered-slot antennas and arrays of such antennas. The fundamental operation of tapered-slot antennas is not yet fully understood, and, for lack of established design rules, the designs of these antennas have been based primarily on empirical results. The document combines results of previous research and development with more-recent design information and measurement data to provide a better understanding of the fundamental operation of tapered-slot antennas and arrays. The document includes a review of typical tapered-slot antenna designs, followed by discussion of fundamental operation (based on physics of the electromagnetic field), analytical methods, and potential applications. Data from recent measurements of field distributions, mutual coupling, and effects of taper profiles on performances of antennas are presented. New feeding techniques and new design concepts for various antenna types are discussed. The document concludes by presenting some examples of active and passive tapered-slot-antenna arrays with potential applications in amplification of power, generation of harmonics, and dynamic scanning of beams. The better understanding provided by the document is intended to contribute to the establishment of design guidelines.

This work was done by Richard Q. Lee of **Lewis Research Center** *and Rainee N. Simons of NYMA, Inc. To obtain a copy of the document, "Tapered Slot Antenna," see TSPs [page 1].*

Inquiries concerning rights for the commercial use of this invention should be addressed to NASA Lewis Research Center, Commercial Technology Office, Attn: Tech Brief Patent Status, Mail Stop 7-3, 21000 Brookpark Road, Cleveland, Ohio 44135. Refer to LEW-16570.

Electronic Systems

Hardware, Techniques, and Processes

13 Automated Vision System Inspects a Large Surface
14 Computer System for Collection of Quality-Assurance Data

Books and Reports

14 Control System for Steerable, Rooftop-Mounted Antenna

BLANK PAGE

Automated Vision System Inspects a Large Surface

Inspection data can be acquired quickly and readily, compared with data from previous inspections.

John F. Kennedy Space Center, Florida

The figure schematically illustrates an automated electronic vision system that operates in conjunction with a scanning robot to inspect a large surface for damage. In the original application for which the system was developed, the surface comprises the panels of the space shuttle thermal radiators, with a total area of more than 1,200 ft² (>111 m²). Typically, the whole area contains between zero and five damage sites, though occasionally it contains hundreds of damage sites, along with hundreds of nondamage sites that may look like damage sites at first glance. Heretofore, the surface was inspected by technicians using flashlights and magnifying glasses in a tedious, slow, labor-intensive process, and the inspection data were recorded manually in a form not readily accessible for review and analysis. The automated vision system performs the inspection much faster and stores results in a data base that is readily accessible for review and analysis.

The system includes a high-resolution video camera mounted on the scanning robot arm, along with two stroboscopic illuminators, about 2 ft (0.6 m) away from the surface to be inspected. The camera and illuminators operate under control by a computer, and the video output is digitized and sent to the computer. The system scans the surface in a continuous motion, viewing a square area about 5 in. (13 cm) on a side. Data are taken when the stroboscopic illuminators "freeze" the motion at intervals of 4 in. (10 cm) along the surface.

The two illuminators are used to reveal different kinds of damage. One illuminator comprises a ring flash lamp that encircles the camera, plus an ellipsoidal reflector behind the camera and flash lamp. The camera and flash lamp lie in one focal plane of the ellipsoid, and the surface to be inspected lies midway between the two focal planes of the ellipsoid. Thus, the surface is illuminated diffusely and nearly uniformly and light reflected from the surface fills the camera lens nearly uniformly over the entire field of view. This optical arrangement provides a bright field illumination system that highlights small damage sites over an extended inspection area. This illuminator is used along with a component of image-data-analysis software to find such microscopic damage as punctures and scratches. The software implements a number of steps in which image background clutter is filtered out and each damage or nondamage site is characterized in terms of a list of specific features that include location, size, and shape. The lists of features for all sites are stored in the data base and the rest of the image data are discarded.

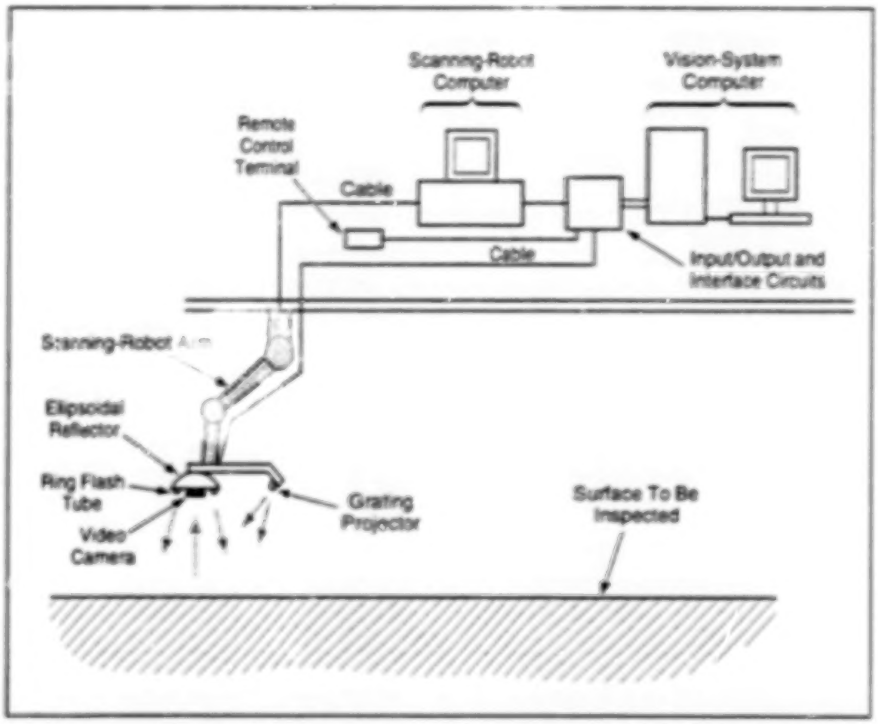

The **Automated Electronic Vision System** and the scanning robot together constitute an automated inspection system that can quickly find a few damage sites on a large surface.

The other illuminator incorporates slide-projector optics and is located on a boom about 2 ft (0.6 m) to one side of the camera. This illuminator projects a grating (that is, a grid pattern in white light, not to be confused with a diffraction grating) onto the surface to be inspected. The resulting image of the grid is processed by a component of image-data-analysis software to find such macroscopic damage as large dents and tape delaminations. The software first processes the image of the grating to obtain the digital equivalent of a depth map of the surface. The depth-map data are then processed in a manner similar to that of the diffuse-illumination-image data to filter out background clutter, characterize each damage or nondamage site in terms of a list of specific features, and store the list of features in the data base.

The problem of identifying relatively few damage sites is solved relatively easily by use of this system. An initial inspection generates a nondamage portion of the data base. The computer can then compare feature data acquired in subsequent inspections with this portion of the data base to find changes indicative of damage that has occurred in the interim.

This work was done by Edward D. Huber and Rick A. Williams of Lockheed Martin Missiles & Space Co. for **Kennedy Space Center**. *Further information is contained in a TSP [see page 1].*

Title to this invention, covered by U.S. Patent No. 5,608,215 has been waived under the provisions of the National Aeronautics and Space Act (42 U.S.C. 2457 (f)). Inquiries concerning licenses for its commercial development should be addressed to

Edward D. Huber
Lockheed Martin Missiles & Space Co., Inc.
Dept. H1-52, Bldg. 202
Advanced Technology Center
3251 Hanover St.
Palo Alto, CA 94304
(650) 424-3308

Refer to KSC-11726, volume and number of this NASA Tech Briefs issue, and the page number.

Computer System for Collection of Quality-Assurance Data

Data are recorded on portable pen computers instead of paper forms.

John F. Kennedy Space Center, Florida

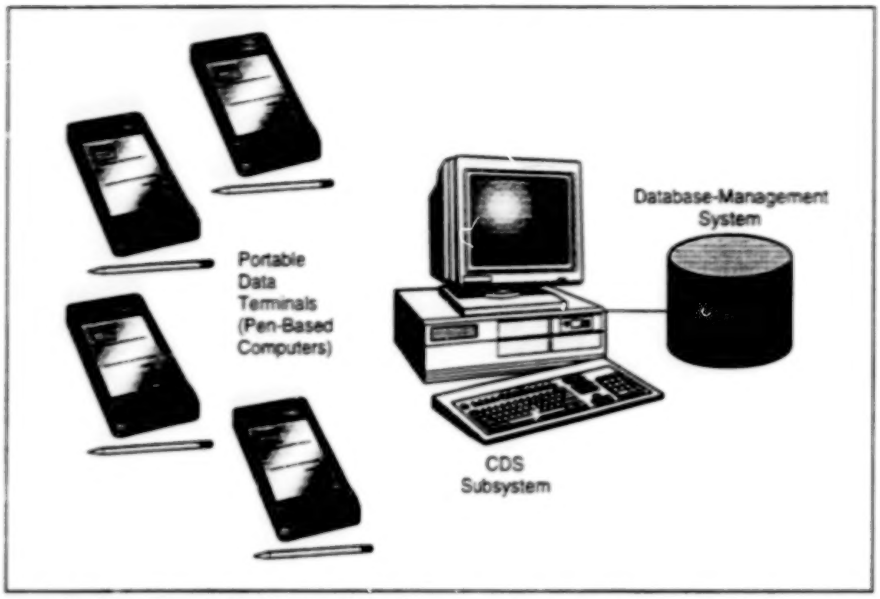

Portable Data Terminals take the place of paper inspection forms. These terminals communicate with the CDS subsystem.

The Paperless Procedure System (PPS) is a computer-based, semiautomated electronic system for collection and management of quality-assurance data in a large organization. The original version of PPS was designed for use by Kennedy Space Center personnel engaged in inspection tasks during test and assembly procedures that are part of preparing the space shuttle and its payloads for flight. The PPS was also designed to be adaptable to nonaerospace commercial applications.

The PPS serves a need to increase productivity and improve the availability of inspection data while maintaining the safety and quality of service in the face of reductions in the number of workers. Heretofore, data from inspections have been written on paper forms, from which the data are subsequently scanned into an archival computer memory in a central database-management system. In the PPS, on the other hand, there is no need for paper forms and the attendant manual processing steps; instead, inspection data are recorded on compact, portable data terminals (pen-based computers) and thereafter processed automatically.

The portable data terminals communicate with a central database server (CDS) subsystem, which includes computer hardware and software performing the functions of a network host and database server (see figure). The PPS makes electronic forms, work-flow-management software tools, and network communication resources accessible to mobile personnel. The most innovative components of the PPS software are the Intelligent Forms Converter (IFC), Data Format Converter (DFC), Inspector's Smart Stamp (ISS™) modules.

The IFC module automates the development of electronic (as distinguished from paper) representations of test and assembly procedures. Unlike in typical other pen-based computer systems, there is no need for a software engineer to reprogram the system and its electronic forms each time the requirements for test and assembly procedure change. Instead, the IFC module accepts, as input, an electronic representation of a test and assembly procedure prepared in a commercial word-processing program. The IFC module then automatically converts the input into the proper electronic format for execution on a pen-based computer.

The DFC module satisfies requirements for preserving all test data, images of inspectors' stamps, notes, deviations, and constraints recorded during a test and assembly procedure that has recently been executed. The DFC converts this recorded information into a final electronic document in a prescribed format. This electronic document is designated an official record of the procedure and is not permitted to be altered subsequently.

The ISS™ module provides an electronic means of authentication analogous to an inspector's ink stamp. The ISS™ module is executed with the help of silicon-based memory devices that store the information necessary for electronic generation of stamp images similar to the ink versions. An inspector causes a stamp image to be generated by touching one of these memory devices to a probe on a portable data terminal.

This work was done by Eric A. Adolphe and Mark Sullivan of Optimus Corp. and Patrick Xantus of Sentel Corp. for **Kennedy Space Center.** *Further information is contained in a TSP [see page 1].*

In accordance with Public Law 96-517, the contractor has elected to retain title to this invention. Inquiries concerning rights for its commercial use should be addressed to

Sentel Corp.
225 Reinekers Lane
Suite 500
Alexandria, VA 22314

Refer to KSC-11943, volume and number of this NASA Tech Briefs *issue, and the page number.*

Books and Reports

Control System for Steerable, Rooftop-Mounted Antenna

An excerpt from JPL Document D-12104 presents additional information on the control system of a steerable microwave antenna that is mounted on the roof of a land vehicle and used to communicate with a geostationary satellite. The antenna and control system were described previously in "Steerable K/Ka-band Antenna for Land-Mobile Satellite Applications" *NASA Tech Briefs*, Vol. 18, No. 1 (January 1994), page 28. Under control by a computer mounted in the vehicle, a motor turns a rotary table to aim the antenna in azimuth toward the satellite, which transmits a pilot-tone signal that serves as an aiming beacon. (The radia-

tion pattern of the antenna is wide enough in elevation so that steering in elevation is unnecessary.) Once the pilot tone has been acquired, an inertial turn-rate sensor mounted in the vehicle provides most of the information needed by an open-loop control subsystem that keeps the antenna pointed toward the satellite as the vehicle moves. Drift of the inertial-sensor bias is the source of most aiming error. Any such error is detected by sinusoidally dithering the rotary table by ±1° at a frequency of 2 Hz while measuring the resulting dither in the strength of the received pilot tone. These measurements are processed into a feedback control signal in a closed-loop control subsystem that responds with a characteristic time of about 10 seconds.

This work was done by Arthur C. Densmore of Caltech and Richard Renner of Cal Corporation for **NASA's Jet Propulsion Laboratory**. *To obtain a copy of the excerpt, "Subsystem Design," see TSPs [page 1].*
NPO-19863

BLANK PAGE

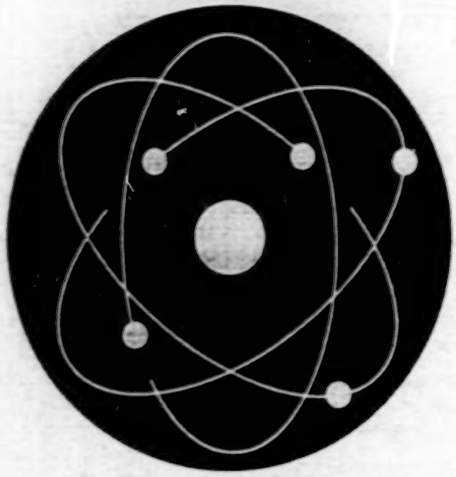

Physical Sciences

Hardware, Techniques, and Processes

19 Chimera/Unstructured Hybrid Grids for Flow and Heat Transfer
20 Source of Fast Oxygen Atoms for Testing Satellite Materials
20 Aircraft-Skin-Rivet Thermocouple

BLANK PAGE

Chimera/Unstructured Hybrid Grids for Flow and Heat Transfer

Flow and heat flux in the flow and bounding structure(s) can be computed together.

Lewis Research Center, Cleveland, Ohio

A hybrid-grid scheme has been developed to afford a computationally efficient means for numerically solving equations of both (1) coupled flows of heat and mass in a fluid and (2) conduction of heat in a body or bodies that bound the fluid. The scheme should prove especially beneficial in analyzing aerodynamic, thermal, and structural effects in turbomachinery.

Among grid methods now in use, the chimera-overset-grid method offers the most flexibility and computational efficiency in representing flows bounded by complexly shaped bodies. A chimera grid is a set of overlapped structured grids that are generated independently and fitted to the body or bodies of interest. A chimera overset grid is a chimera grid that includes (1) a major grid generated about a main body element and (2) minor grids superimposed on the major grid to resolve interesting features of the configuration.

The unstructured-grid method facilitates the solution of problems pertaining to solid bodies (e.g., strain problems). However, the unstructured-grid method does not offer computational efficiency for solving flow and heat-transfer problems.

The present hybrid scheme is intended to take advantage of the strengths of the chimera-overset-grid and unstructured-grid methods. The scheme involves the use of a chimera overset grid in the flow volume, coupled to an unstructured grid or grids for modeling conduction of heat in the bounding body or bodies.

Unlike in older grid schemes and associated numerical-solution methods, in the present scheme, one need not assume physically unrealistic prescribed heat fluxes (e.g., zero heat flux in the traditional adiabatic-wall assumption) or constant temperatures at fluid/solid interfaces. Instead, the heat fluxes in the fluid and solid are treated more realistically as unknowns that are coupled to each other; following a conjugate-analysis approach, the temperatures and heat fluxes are required to be continuous across fluid/solid interfaces. In this scheme, one performs a conjugate analysis, wherein the mass flow and the heat fluxes are treated as parts of integral system, the equations of which can be efficiently solved together to obtain aerodynamic, thermal, and structural effects.

The scheme has been tested by using it to compute flows about, and distributions of temperature, within a cooled flat plate and a turbine cascade with 10 cooling holes per blade (see figure). The results of these computations are in substantial agreement with results of experiments. In the foregoing computations and in other computations for a simplified drum/disk structure, conduction of heat in solid bodies has been shown to affect surface temperatures in that these temperatures differ from those computed with the adiabatic-wall assumption.

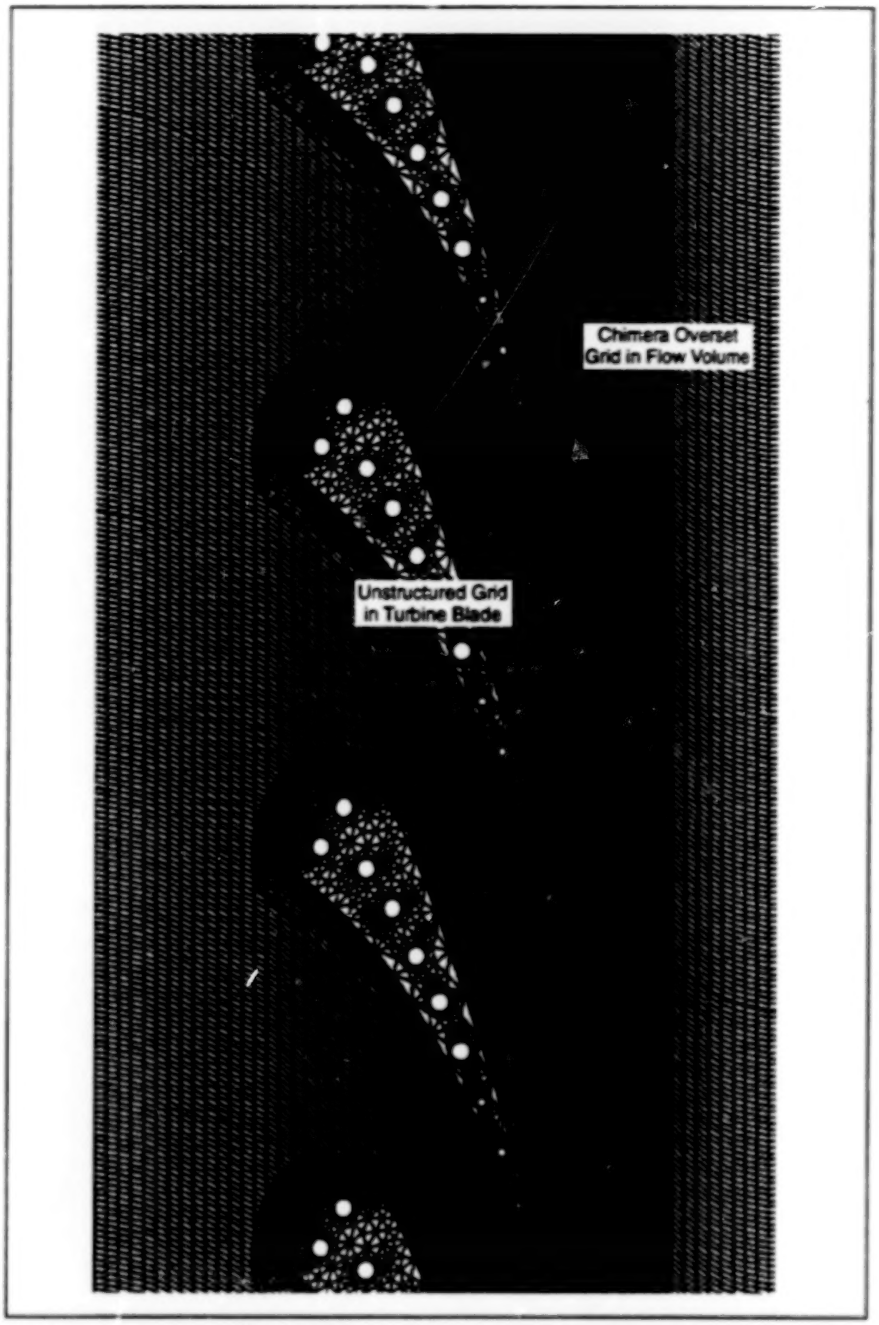

A Chimera/Unstructured Hybrid Grid enables the computational treatment of a turbine cascade as one integral system, for which the coupled equations of aerodynamic, thermal, and structural effects can be solved together.

This work was done by Meng-Sing Liou of **Lewis Research Center** *and Kai-Hsiung Kao of the Institute for Computational Fluid Mechanics in Propulsion. Further information is contained in a TSP [see page 1].*

Inquiries concerning rights for the commercial use of this invention should be addressed to NASA Lewis Research Center, Commercial Technology Office, Attn: Tech Brief Patent Status, Mail Stop 7–3, 21000 Brookpark Road, Cleveland, Ohio 44135. Refer to LEW-16431.

Source of Fast Oxygen Atoms for Testing Satellite Materials

A high-flux source of 8-km/s oxygen atoms can be used to evaluate aging of materials in near-Earth outer space.

Physical Sciences Inc., Andover, MA

Fast O-Beam Properties	
Velocity	8 km/s ± 15% (5 to 12 km/s range)
Fluence	~10^{18} O-atoms/pulse, 3 Hz
Composition	>80% oxygen atoms
Size	Expandable to >1,000 cm^2 area
Charge content	<1% ions (controllable by pseudo-Helmholtz coils)
Metastable content	$O(^1D)$ concentration <0.4%
Temperature	T = 300 K
VUV/UV content	One photon per 10^4 O atoms (similar to LEO)

A **Summary** highlights the properties of the O-Beam.

We have developed an apparatus that generates a pulsed beam of fast oxygen atoms, under Small Business Innovation Research (SBIR) funding by NASA's Jet Propulsion Laboratory, to provide a ground test facility to qualify materials to be used in low Earth orbit (LEO). This development was in response to a number of early space-shuttle observations of material erosion and property change resulting from interaction with the LEO atmosphere, which is predominantly monatomic oxygen. These interactions occur at orbital speeds ≈8 km/s. To our knowledge, ours is the only system that provides a high-flux beam of neutral oxygen atoms with wide-area operating capability at the desired speed of 8 km/s. Sets of materials (2.5-by-2.5-cm samples) have been simultaneously bombarded by 8-km/s oxygen atoms at fluences of up to 6×10^{21} cm^{-2} in our facility.

The hyperthermal-oxygen-atom source is housed in two stainless-steel six-way crosses, including an 8-in. (20-cm) cross source chamber housing a pulsed oxygen-valve/nozzle assembly, connected to a 16-in. (41-cm) cross expansion chamber. A cryopump attached to the large cross maintains a base pressure of 3×10^{-7} torr (4×10^{-5} Pa).

The oxygen atoms are generated in a pulsed laser discharge in pure O_2. A 12-J/pulse CO_2 laser is focused into a conical expansion nozzle, which has been partially filled with O_2 by a pulsed-beam valve. The resulting plasma, ignited at the throat, expands out the nozzle, dissociating the molecular oxygen in front of it. The nozzle was designed to allow recombination of ions and electrons while the slower kinetics of atom/atom recombination maintains a highly dissociated beam. The result, at 8 km/s, is an approximately 50-μs pulse of highly dissociated oxygen (>80 percent atoms) with less than 1 percent ion content (the beam is charge-neutral).

The speed (5 to 12 km/s) of atoms in the beam is selected by varying the time delay between the pulsing of the O_2 valve and the triggering of the CO_2 laser. The delay determines the mass of O_2 processed by the pulsed discharge; this mass is inversely related to the speed of the atoms in the beam.

The fidelity of the LEO simulation is critical for evaluation of materials, and so considerable effort has been expended in characterizing the beam. The measured beam properties are summarized in the accompanying table. A variety of diagnostics have been developed for use with the system.

Our O-beam facility has been employed on several occasions to pretest materials that were subsequently flown in space experiments. The ground-test data and flight-test data were found to be in substantial agreement. A most recent large ground test was for the SEE (Space Environments and Effects) program on materials for the EOIM-3 (Evaluation of Oxygen Interactions with Materials Experiment–3) flight. We irradiated 84 materials following a careful protocol of pre- and post-test weighing. The Jet Propulsion Laboratory performed subsequent surface analysis. With a few understood exceptions, as before, the ground-test and flight-test results for these materials were found to be in substantial agreement, demonstrating our ability to simulate LEO conditions.

Our facility is used to provide material-evaluation services. To date, we have tested over 2,000 samples for both government and industrial customers. The facility has also been utilized to investigate other phenomena of importance to LEO operations, including contamination cleanup, scattering distributions and accommodation coefficients, shuttle glow, and excitation of emissions from contaminant gasses.

The basic concept of the fast-atomic-oxygen source has been extended to form fast atomic beams of other species; for example, fluorine, chlorine, and nitrogen atoms, for potential applications in the semiconductor industry.

Physical Sciences Inc. designs, builds, and licenses customized versions of our fast-atom source. Such systems are presently operational at the Center for Studies in Research and Technology, in Toulouse, France and The European Space Research and Technology Center in Noordwijk, The Netherlands. A system has also recently been delivered to NASDA Tsukuba Space Center in Japan.

This work was performed by George Caledonia and Robert Krech of **Physical Sciences Inc.** *under SBIR contract monitored by* **NASA's Jet Propulsion Laboratory**. *For more information, please call (978) 689-0003 or E-mail to caledonia@psicorp.com.*
SBIR0003

Aircraft-Skin-Rivet Thermocouple

This device measures temperature without disturbing airflow.

Lewis Research Center, Cleveland, Ohio

The aircraft-skin-rivet thermocouple is designed for measuring the temperature on the outer surface of an airplane wing under icing conditions. More specifically, its design was motivated by the need to measure the temperature near 32 °F (0 °C) on an aluminum wing skin, with an error of no more than 1 °F (0.6 °C), without disturbing the airflow over the wing.

As its name suggests, the aircraft-skin-rivet thermocouple is a thermocouple embedded in an aircraft-skin rivet, with

connections to thermocouple wires routed inside the wing. This design satisfies a requirement for simplicity of installation in the field, without need for access to the interior of the wing (other than for routing and connection of the thermocouple wires). Inasmuch as rivets are used in any event to hold the skin in place, this design satisfies a requirement for compatibility with the skin. Like the other rivets on the wing, the one that holds the thermocouple is made flush with the surface upon installation and therefore does not introduce any surface alteration that would disturb the airflow.

At the time of reporting the information for this article, measurements and calculations to determine the accuracy of the aircraft-skin-rivet thermocouple had not been completed. However, preliminary estimates had been interpreted as signifying that the thermocouple readings would eventually be found to be accurate within less than the design error.

This work was done by David W. Sheldon and Dean R. Miller of **Lewis Research Center**. *Further information is contained in a TSP [see page 1].*

Inquiries concerning rights for the commercial use of this invention should be addressed to NASA Lewis Research Center, Commercial Technology Office, Attn: Tech Brief Patent Status, Mail Stop 7–3, 21000 Brookpark Road, Cleveland, Ohio 44135. Refer to LEW-16397.

BLANK PAGE

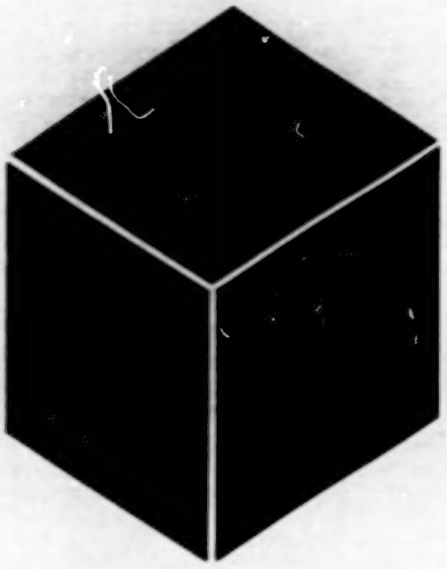

Materials

Hardware, Techniques, and Processes

25 Advanced Cryogenic Insulation System for Graphite/Organic Resin Composite Cryogenic-Tank Structures
26 Nearly Isotropic Resin-Transfer-Molded Composites
26 Joining of SiC-Based Ceramic and Fiber-Reinforced Composite Parts
27 Better Electrochemical Profiling of III–V Semiconductors
28 Fiber-Reinforced-Plastic/Concrete Structural Members
29 High-T_g Thermosetting Polyimide
29 Reflective Coating System for High-Temperature Vacuum Use
30 Creep-Resistant Ceramic Composite for High-Temperature Use
30 Iron-Containing Carbon Materials Made From Graphite Fluoride

Books and Reports

32 Evaluation of Additives to PFPEs in Boundary Lubrication

BLANK PAGE

Advanced Cryogenic Insulation System for Graphite/Organic Resin Composite Cryogenic-Tank Structures

Foam-filled honeycomb cores withstand tensile strain test in cryogenic conditions.

Marshall Space Flight Center, Alabama

Engineers at Rockwell International Corporation's Space System Division have developed a new method of insulating composite structural material that will stand up to the harsh environment of space. The new liquid-hydrogen cryogenic tankage proposed for advanced launch systems — such as the Reusable Launch Vehicle and the X-33 — will be made from a graphite/epoxy material. Although this composite material will produce a lighter-weight cryogenic insulation tank, current cryogenic insulation materials did not endure rigorous stress testing.

Conventional cryogenic tankage (such as the external tank of the space shuttle, and those used on the Saturn SII, SIVB, and Atlas Centaur) are commonly made of aluminum or stainless-steel alloys. Cryogenic insulation materials for these types of tanks consist of monolithic forms of polyurethane foam or an organic spray-on or bonded insulation. These rigid insulation materials proved to be incompatible with graphite composite material at –423 °F (–253 °C) — the cryogenic temperature of liquid hydrogen.

Rockwell engineers called upon previous experience with bonding honeycomb cores to graphite fiber/resin matrix composites, knowing that honeycomb core materials will allow for subtle shifts in the composite and insulation material without bond or shear failure. This "flexibility" is possible because of the accordionlike construction of the honeycomb core and good adhesion to the composite material.

Cryogenic-tank insulation systems for future launch vehicles also called for insulation that could withstand a maximum 400 °F (204 °C) at the thermal-protection-system interface. Additionally, the core/foam/composite interfaces at the tank wall must be sealed to prevent cryo-pumping.

Because no current pour or spray-in-place insulation materials were available to meet these requirements, engineers decided to combine a 2.0-lb/ft^3 (32-kg/m^3) polymethacrylimide foam sheet (Rohacell 31A or equivalent) with a 2.0-lb/ft^3 (32-kg/m^3) polyurethane spray foam (PDL 1034-141B or equivalent) for temperatures less than 300 °F (150 °C).

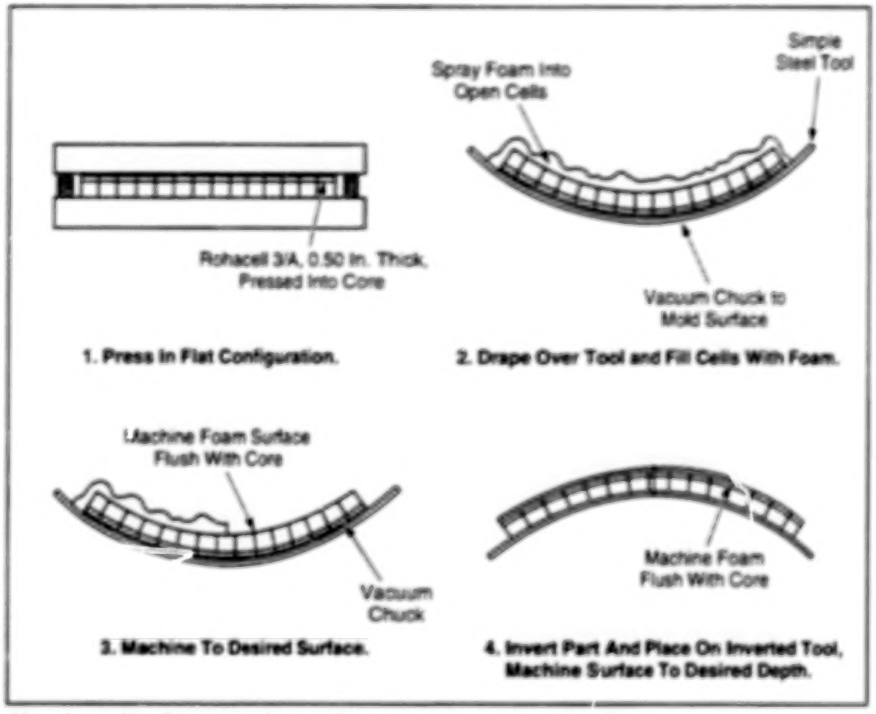
Spray Foam Into Open Cells
Simple Steel Tool
Rohacell 3/A, 0.50 In. Thick, Pressed Into Core
Vacuum Chuck to Mold Surface
1. Press In Flat Configuration.
2. Drape Over Tool and Fill Cells With Foam.
Machine Foam Surface Flush With Core
Vacuum Chuck
Machine Foam Flush With Core
3. Machine To Desired Surface.
4. Invert Part And Place On Inverted Tool, Machine Surface To Desired Depth.

Manufacturing Sequence for installing foam into honeycomb core.

This foam combination is accomplished by pressing the Rohacell 31A sheet into the knife edges of one side of the honeycomb core like a cookie cutter. The foam is pressed to the predetermined 300 °F (150 °C) interface. The partially filled core is then inverted, with the bare cells facing up. Next, the Rohacell 31A foam surface is edge-sealed and vacuum-chucked to a curved tool surface representing the curvature of the tank wall. The open cells are then filled with polyurethane spray foam using standard Gussmer pumps and Binks mixing gun equipment. The excess foam material is machined flush with the core cells to the tank contour while still under vacuum from the spray-foam operation. This insulation assembly is then inverted, vacuum chucked to the contour of the convex tool surface, and machined to the final interface contour and thickness.

The completed insulation panels are bonded to the tank-wall surface with a polyurethane adhesive that cures at room temperature (Crest 212 modified with silane Z6040 coupling agent or equivalent). The bonding process involves vacuum-bagging the insulation panel directly to the tank wall and curing the adhesive for at least eight hours prior to releasing the pressure. The total cure time of the adhesive at room temperature is 48 hours.

The process of forming and testing this advanced cryogenic insulation system has been recorded on a videotape, titled "Composite Hydrogen Tank Foam Process for SSTO," tape number 1-9506-09.

This work was done by Jeff D. Eichinger, Richard G. Jackson, John (Jack) S. Jones, Conley S. Thatcher, and Dave Wittman of Rockwell International Corporation for the **Marshall Space Flight Center**. *Further information is contained in a TSP [see page 1].*
MFS-31108

Nearly Isotropic Resin-Transfer-Molded Composites

Unlike older resin-transfer-molded composites, these can be machined in fine detail.

NASA's Jet Propulsion Laboratory, Pasadena, California

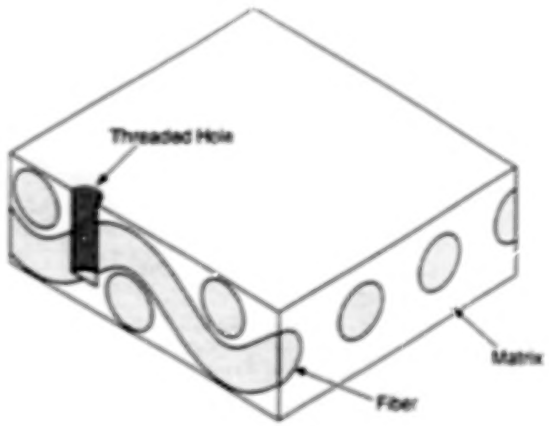

OLDER-STYLE COMPOSITE BLOCK CONTAINING PREFORM WITH COARSE BRAID

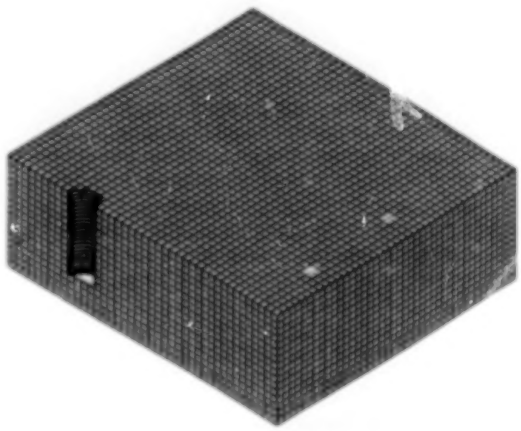

NEWER-STYLE COMPOSITE BLOCK CONTAINING PREFORM WITH FINE WEAVE

The Fine Weave of the newer composite is more conducive to fine machining and to retention of strength in fine details like screw threads.

Nearly isotropic matrix/fiber composite materials can be made quickly and at relatively low cost by resin-transfer molding. The fiber components of these materials are fine, loosely woven, three-dimensional preforms; the matrix components are epoxy or polycyanate resins. With proper tooling, these materials can be resin-transfer molded to net shape. Alternatively, they can be machined to net shape. The three-dimensional weaves enable the materials to withstand machining with minimal loss of mechanical properties. These materials are particularly suitable for lightweight, all-composite replacements for aluminum end fittings that have been used on tubular composite-material structural members.

Heretofore, resin-transfer-molded composites have been made with relatively coarse three-dimensional braided or angle-interlock woven preforms (see figure). These composites are so coarse that they cannot be machined and cannot be fabricated with fine details. For example, screw threads in these materials are useless because the threads contain no reinforcement and thus have insufficient strength.

The fine three-dimensional weaves of the present composites were developed previously for carbon/carbon composites, but have not been used heretofore in resin-transfer-molded composites. The method used heretofore to make carbon/carbon composites requires long processing times and expensive capital equipment, and the materials produced by this method are too brittle at room temperature to satisfy the requirements that prompted the development of the present nearly isotropic resin-transfer-molded materials.

The three-dimensional loosely woven preforms used in the present materials cost less than do the coarser three-dimensional preforms made by conventional three-dimensional braiding or weaving. In comparison with the coarser three-dimensional woven preforms, the present finer preforms are weaker on a large scale but stronger on a small scale like that of screw threads, where the fine weaves provide reinforcement that the coarser weaves cannot.

This work was done by D. Kyle Brown of Caltech for **NASA's Jet Propulsion Laboratory**. *Further information is contained in a TSP [see page 1].*
NPO-19918

Joining of SiC-Based Ceramic and Fiber-Reinforced Composite Parts

Thermomechanical properties of joints can be tailored.

Lewis Research Center, Cleveland, Ohio

A process that involves reaction forming has been devised to enable the joining of high-temperature-resistant structural parts made of SiC-based materials. These materials include SiC-based ceramics and composites reinforced by fibers that are made of various component materials and are woven, wound, or otherwise arranged in various configurations. The technique can be used to join simply shaped parts to make complexly shaped structures, and to repair such parts and structures.

The process begins with the application of a carbonaceous mixture to the joint regions between parts. The mixture is cured at a temperature between 90 and 110 °C. The joints are then locally infiltrated with molten silicon or with alloy(s) of silicon and refractory metal(s). The molten silicon or alloy reacts with the carbon in the joint to form silicon carbide with amounts of silicon and refractory disilicide phases that can be tailored by choice of the compositions of the reactants. Consequently, the process

results in joints with tailorable microstructures and thus tailorable thermomechanical properties. The properties of the joints can be tailored to approximate closely those of the joined parts.

The figure shows some examples of SiC-based ceramic and fiber-reinforced composite parts that were joined by use of this process. In mechanical tests, the joints on these parts were found to retain their strength at temperatures from ambient up to 1,370 °C. The test temperature of 1,370 °C is above the maximum to which the parts are expected to be exposed in use.

This work was done by Mrityunjay Singh of NYMA, Inc., for **Lewis Research Center**. *Further information is contained in a TSP [see page 1].*

Inquiries concerning rights for the commercial use of this invention should be addressed to NASA Lewis Research Center, Commercial Technology Office, Attn: Tech Brief Patent Status, Mail Stop 7–3, 21000 Brookpark Road, Cleveland, Ohio 44135. Refer to LEW-16405.

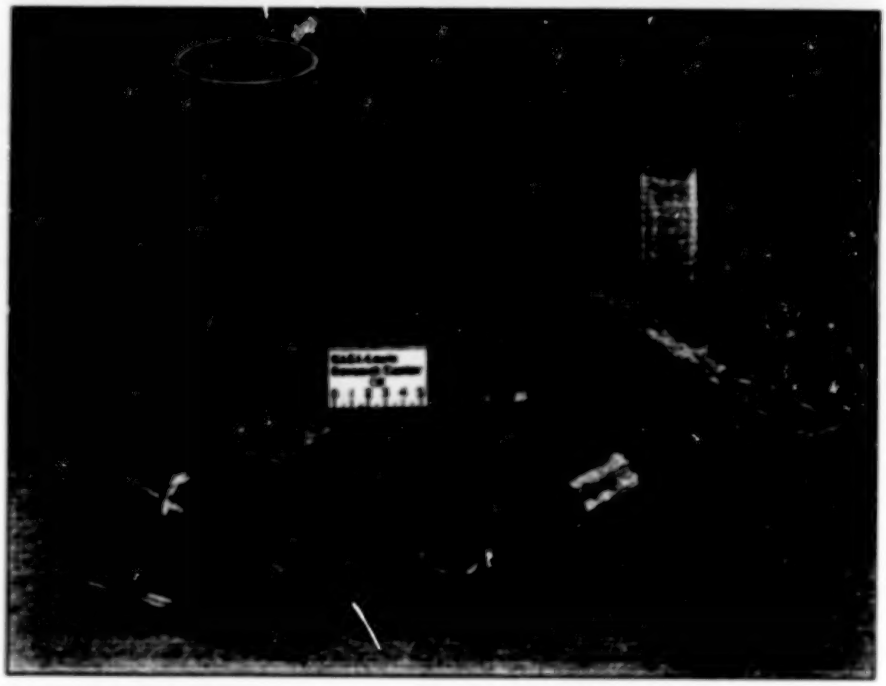

Simpler Parts Were Joined to form more-complex parts by the joining process described in the text.

Better Electrochemical Profiling of III–V Semiconductors

An improved solution can be used on a greater variety of materials.

Lewis Research Center, Cleveland, Ohio

An etching and electrolyte solution called "UNIEL" has been found to be useful for electrochemical characterization as a function of depth ("electrochemical profiling" for short) of semiconductor compounds of elements from periods III and V of the periodic table; that is, InP- and GaAs-based semiconductors. UNIEL is a mixture of three solutions denoted A, B, and C in the volume proportions of 1, 4, and 1, respectively. The compositions of these solutions are the following:

- Solution A: 5 parts by volume of a 48-percent aqueous solution of hydrofluoric acid + 1 part by volume of a 99-percent aqueous solution of acetic acid + 2 parts by volume of an 85-percent solution of ortho-phosphoric acid + 100 parts by volume of water;
- Solution B: 0.1 molar N-n- butylpyridinium chloride; and
- Solution C: 1 molar NH_4F_2.

Electrochemical profiling can contribute to characterization and thus to the development of layered InP- and GaAs-based semiconductor device structures for photovoltaic cells. Current-vs.-voltage, capacitance-vs.-voltage, and conductance-vs.-voltage characteristics obtained by electrochemical profiling can be used to determine surface and bulk semiconductor properties like diffusion length, lifetime of minority charge carriers, surface recombination velocity, and concentration of majority charge carriers at any depth (see figure).

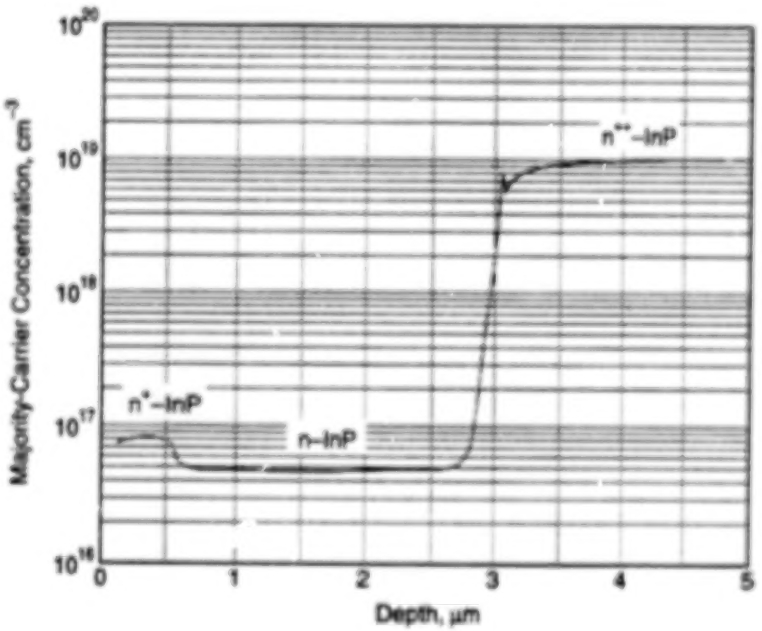

The Majority-Carrier Concentration of a specimen of n^{+}-doped InP deposited on n-doped InP deposited on n^{++}-doped InP substrate was determined by electrochemical profiling in the UNIEL solution.

Prior to the development of UNIEL, six other solutions had been used for chemical profiling solutions of III–V semiconductors. None of the previously developed solutions

had been found to be useful on all III–V semiconductor compounds, and neither has UNIEL. However, of all the solutions, UNIEL appears to be useful on the greatest variety of III–V compounds. In particular, it has yielded very good results in tests on n- and p-doped InP and GaAs substrates and homo- and heterostructures made of InP, GaAs, InGaAs, and InGaAsP layers. Preliminary studies have also shown that similar electrolytes based on UNIEL work fairly well for profiling GaP, AlGaP (with high Al content) and InGaSbP epitaxial layers, even with Si and Ge substrates.

This work was done by Maria Faur, Dennis J. Flood, Philip P. Jenkins, and David M. Wilt of **Lewis Research Center** *and Mircea Faur and Manju Goradia of Cleveland State University. Further information is contained in a TSP [see page 1].*

Inquiries concerning rights for the commercial use of this invention should be addressed to NASA Lewis Research Center, Commercial Technology Office, Attn: Tech Brief Patent Status, Mail Stop 7–3, 21000 Brookpark Road, Cleveland, Ohio 44135. Refer to LEW-16509.

Fiber-Reinforced-Plastic/Concrete Structural Members

Strength and durability are enhanced.

John F. Kennedy Space Center, Florida

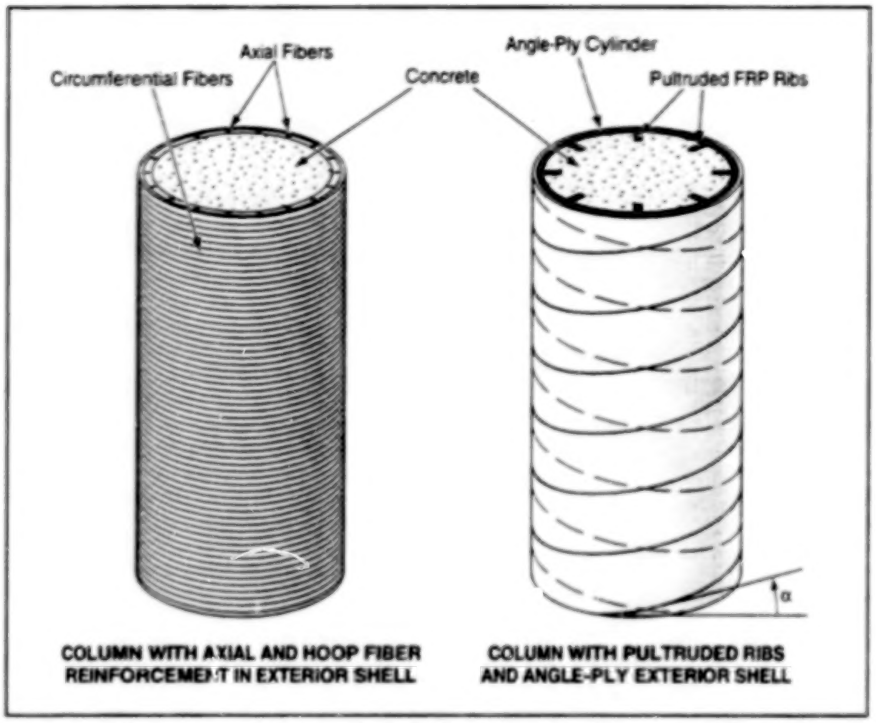

Concrete Columns can be fabricated with FRP exterior shells. Optionally, FRP ribs or other reinforcing FRP interior components can be included. The two configurations shown here are only typical; many other configurations are also possible.

Improved concrete structural members such as columns, piers, and piles can be manufactured by incorporating fiber-reinforced-plastic (FRP) exterior shells and FRP interior submembers. The FRP components impart greater compressive, flexural and shear strengths and ductility to a concrete structural member, relative to a similar concrete structural member made in the conventional way, without FRP. During fabrication, the FRP exterior shell also serves as a form for casting the concrete. Moreover, during use of the structure, the FRP exterior shell prevents or retards the intrusion of moisture, thereby helping to prevent or retard both environmental degradation of the concrete and corrosion of any steel reinforcement or steel structural member(s) embedded or anchored in the concrete. Thus, concrete structural members made with FRP offer greater strength and durability that should be especially advantageous for bridges and similar structures in hurricane-prone coastal areas, earthquake zones, and regions where moist concrete is damaged during freeze/thaw cycles.

Concrete structural members incorporating FRP components can be made in a wide variety of configurations, using a wide variety of polymer-matrix/fiber composite materials and composite-fabrication processes, and various concretes with or without conventional steel or advanced fiber reinforcement. A typical FRP comprises about 60 percent fibers (e.g., glass, carbon, or aromatic polyamid) and 40 percent polymeric matrix material (e.g., a polyester, vinylester, or epoxy). The concrete can be cast at the construction site, or it can be cast in a factory, possibly using centrifugation to enhance the bond between the concrete and the exterior shell.

The figure illustrates some typical configurations for a round column with an FRP tube as the exterior shell, with or without interior FRP reinforcement. The shell can be made in two or more layers; for example, an inner layer containing axial fibers and an outer layer containing circumferential (hoop) fibers, both layers fabricated in a continuous filament-winding process. The ribs (if any) can be made by pultrusion. The axial fibers (if any) increase the flexural capacity of the column. Inward buckling of the axial fibers is inhibited by the concrete core. The hoop reinforcement confines the concrete and prevents outward bucking of both the axial fibers and of any longitudinal interior reinforcing ribs or bars. Alternatively, the exterior shell can be fabricated in a multilayer angle-ply configuration with winding angles of $\pm\alpha$, or as a sandwich of axial fibers between two hoop layers.

The interior FRP reinforcement can be in any of various forms; for example, ribs or H-columns, or else bars or cages like those of conventional steel reinforcements. A particularly advantageous design calls for pultruded longitudinal ribs formed integrally within a pultruded tube covered by an angle-ply laminate, as shown on the right side of the figure. This design can reduce or even eliminate the need for a conventional steel reinforcing cage embedded in the column, thereby reducing the time and cost of construction and enhancing durability in a saltwater or other corrosive environment.

This work was done by Amir Mirmiran of the University of Central Florida and Moshen Shahawy of the Florida Department of Transportation for **Kennedy Space Center**. *Further information is contained in a TSP [see page 1].*
KSC-11946

High-T_g Thermosetting Polyimide

A less-toxic monomer is substituted for the monomer of the industry standard polyimide.

Lewis Research Center, Cleveland, Ohio

A thermosetting polyimide called "DMBZ-15" has been developed for use as a matrix material in relatively inexpensive matrix/fiber composite materials. The glass-transition temperature (T_g) of DMBZ-15 is 414 °C. In contrast, the industry standard polyimide for such composites (developed in 1971 at Lewis Research center and known as "PMR-15") has a T_g of 348 °C. Because of its higher T_g, DMBZ-15 is better suited for high-temperature use in automotive and aerospace applications.

The development of DMBZ-15 began as a search for an alternative to the toxic monomer — methylene dianiline (MDA) — used to make PMR-15. The objective of the search was to substitute a more benign diamine for MDA, while maintaining composite material performance comparable to that of composites made with PMR-15. The search led to the ingredients of DMBZ-15; namely, dimethyl ester of 3,3',4,4'-benzophenone tetracarboxylic acid (BTDE) and 2,2'-dimethylbenzidine (DMBZ) with nadic ester (NE) as the end cap.

Experiments were performed on composite material specimens made with PMR-15 and DMBZ-15 matrices, respectively, reinforced with carbon fibers known by the trade name "T650-35." In one set of experiments, flexural strengths were measured at room temperature and at 550 °F (288 °C). In another set of experiments, compressive strengths were measured at various temperatures up to 550 °F (288 °C). In still another set of experiments, measurements of compressive strength were performed after five "hot/wet" cycles; each cycle comprised (1) a soak in water at 200 °F (93 °C) until a weight gain >1 percent was detected, followed by (2) drying at a temperature of 500 °F (260 °C) until the moisture level was reduced to <0.1 percent of the specimen weight. As shown in the figure, specimens of the two composites tested under the same conditions exhibited comparable levels of flexural and compressive strengths.

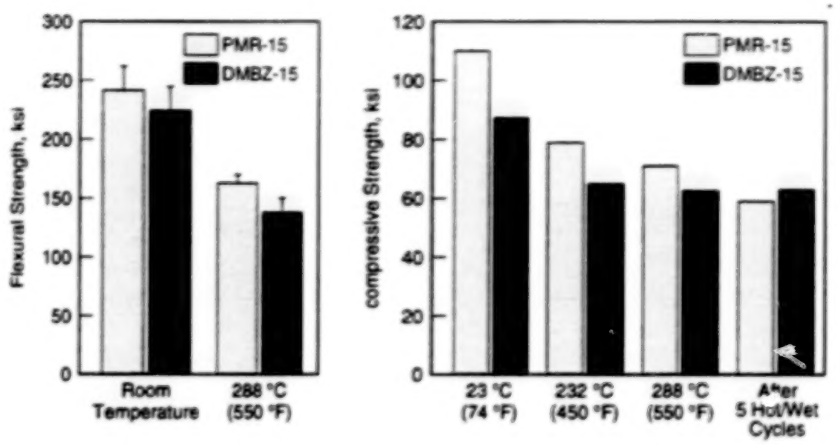

DMBZ-15/Carbon Fiber and PMR-15/Carbon Fiber Composites exhibited similar levels of flexural and compressive strengths.

This work was done by Kathy C. Chuang of **Lewis Research Center**, *Joseph E. Waters of Case Western Reserve University, and DeNise Hardy-Green of the University of Akron. No further documentation is available.*

Inquiries concerning rights for the commercial use of this invention should be addressed to NASA Lewis Research Center, Commercial Technology Office, Attn: Tech Brief Patent Status, Mail Stop 7–3, 21000 Brookpark Road, Cleveland, Ohio 44135. Refer to LEW-16560.

Reflective Coating System for High-Temperature Vacuum Use

This system retains its reflectivity after heating to 500 °C.

Lewis Research Center, Cleveland, Ohio

A substrate of nickel coated with a thin layer of silver and further coated with a thin protective layer of silicon dioxide has been found to constitute an optically reflective substrate/coating system that is suitable for use at high temperature in vacuum. This system was developed originally for use on space solar dynamic and solar thermal power systems and, in particular, on secondary solar-radiation concentrators, which are expected to operate at temperatures in the range of 400 to 800 °C. This substrate/coating system might also be applicable to hot optical components of terrestrial solar electric-power systems, solar-powered wastewater-treatment systems, solar-powered fiber-optic illumination systems, and laboratory optical instruments.

The predecessors to this substrate/coating system include a pure silver substrate diamond-turned to a mirror finish, a pure copper substrate coated with silver, and a single-crystal sapphire substrate coated with silver. After heating to 450 °C, the pure silver substrate exhibited severe grain-boundary growth, which rendered the surface diffuse. After heating to 420 °C, the copper-substrate/silver system exhibited diffusion of silver into the copper, rendering the surface layer silver poor. The sapphire/silver system exhibited excellent

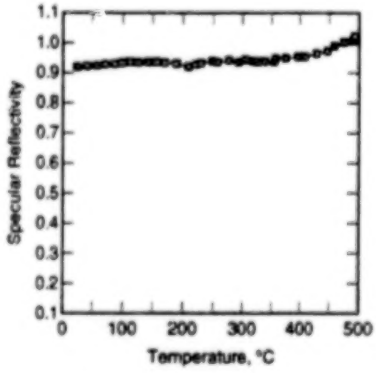

A Sample Retained High Specular Reflectivity during heating over a wide temperature range.

reflectivity characteristics when heated to 530 °C, but this system was deemed impractical because sapphire would be difficult to form into the shape of a secondary concentrator.

Silver has long been the reflective coating material of choice for use at room temperature. The present SiO_2-on-Ag-on-Ni substrate/coating system retains its reflectivity at high temperature, at least partly because with nickel as the substrate, little or no silver diffuses into the substrate. Moreover, the nickel substrate can readily be machined to a desired shape and can be either metallurgically polished or diamond-turned to a mirror finish.

Initial samples of this substrate/coating system were fabricated by polishing nickel substrates to a mirror finish, followed by electron-beam evaporation (alternatively, sputtering could be used) to deposit silver to a thickness of 1,000 Å, followed by deposition of SiO_2 to a thickness of 1,000 Å. During a test of the first sample, the specular reflectivity was found not to change appreciably as the sample was heated from room temperature to almost 500 °C (see figure). Microscopic examination of a sample that had been heated to 798.5 °C revealed many small grains — too small to affect the reflectivity.

The smallness of the grains may be a fortuitous result of the thinness of the silver layer. It has been conjectured that the sizes of the grains might increase with the thickness of the silver. Thus, there might be an upper limit to the desired silver thickness, beyond which the specular reflectivity could be degraded by the formation of larger grains. Apparently, the upper limit is greater than the 1,000 Å of the initial samples. Optionally, one might select greater thicknesses of silver to promote the formation of larger grains in order to obtain diffusely reflective high-temperature coating/substrate combinations for use in optical components (e.g., integrating spheres) for capturing and diffusing light at high temperatures.

This work was done by Donald A. Jaworske of **Lewis Research Center**. *Further information is contained in a TSP [see page 1].*

Inquiries concerning rights for the commercial use of this invention should be addressed to NASA Lewis Research Center, Commercial Technology Office, Attn: Tech Brief Patent Status, Mail Stop 7–3, 21000 Brookpark Road, Cleveland, Ohio 44135. Refer to LEW-16411.

Creep-Resistant Ceramic Composite for High-Temperature Use

Alumina, silica, and mullite are combined into an improved matrix material.

Lewis Research Center, Cleveland, Ohio

A low-density, creep-resistant ceramic composite material has been developed as a prototype of such materials for use at high temperatures in the next generation of aircraft engines. The material consists of Nextel (or equivalent) ceramic fibers in a matrix that is, itself, a composite of mullite particles in a mixture of 90 percent alumina with 10 percent silica. In fabricating an article of this material, the matrix is infiltrated into a three-dimensional woven fiber preform by use of sol-gel techniques in a multistep process.

In general, it is desirable to prevent bonding between the matrices and fibers of high-temperature ceramic composite articles to prevent fiber/matrix interactions of a type that can damage the fibers and thereby lead to embrittlement and failure of the articles. To prevent matrix/fiber bonding in the present material, an unstabilized zirconia interfacial layer is deposited on the fibers prior to infiltration with matrix material. Subsequently, the zirconia goes through a phase change with a concomitant volume change as it is heated and again as it is cooled. These volume changes fracture the interfacial layer, thus destroying any matrix/fiber bonds that might have formed.

The infiltration steps provide a matrix of uniformly low density. The initial infiltrating matrix precursor material comprises mullite powder mixed into an alumina/silica sol-gel. The viscosity of the gel keeps the mullite powder in suspension during infiltration. (The viscosity of the gel can be temporarily reduced by an ultrasonic probe to aid infiltration.) The sol is then gelled in situ by use of ammonia gas to cause a change in pH. The gelation step helps to ensure uniform distribution of matrix material throughout the preform by preventing the liquid component of the matrix precursor from migrating away from the interior of the article during drying. The article is then heat-treated above the matrix precursor transition temperature of 526 °F (274 °C).

Further densification is achieved by repeated steps of infiltration with alumina/silica sol-gel followed by heat treatment above the transition temperature. A final heat treatment is performed at the intended use temperature to stabilize the matrix.

In an experiment, the four-point-flexure strength of a specimen of this material was 3.9 kpsi (27 MPa) before and 3.6 kpsi (25 MPa) after exposure to a temperature of 1,800 °F (980 °C) for 100 hours. The corresponding flexure-strength figures for a specimen with an all-alumina matrix were lower; 3.3 kpsi (23 MPa) before and 2 kpsi (14 MPa) after exposure to the same high temperature.

This work was done by Anna L. Baker of United Technologies Pratt & Whitney for **Lewis Research Center**. *Further information is contained in a TSP [see page 1].*

Inquiries concerning rights for the commercial use of this invention should be addressed to NASA Lewis Research Center, Commercial Technology Office, Attn: Tech Brief Patent Status, Mail Stop 7–3, 21000 Brookpark Road, Cleveland, Ohio 44135. Refer to LEW-16248.

Iron-Containing Carbon Materials Made From Graphite Fluoride

Products can include magnetic materials.

Lewis Research Center, Cleveland, Ohio

Experiments have shown that carbon-based materials containing pure metallic iron, alloys of iron, halides of iron, and/or oxides of iron can be synthesized from precursors of general composition CF_x, denoted loosely as graphite fluoride. Typical samples of the product materials contain 1 iron atom per 3.5 to 5 carbon atoms. Those product materials that contain iron in the pure, alloy, and/or Fe_3O_4 forms are magnetic (see figure).

Some earlier related experiments were reported in "Storing Fluorine in Graphitelike Carbon Fibers" (LEW-15359), *NASA Tech Briefs*, Vol. 19, No. 12 (December 1995).

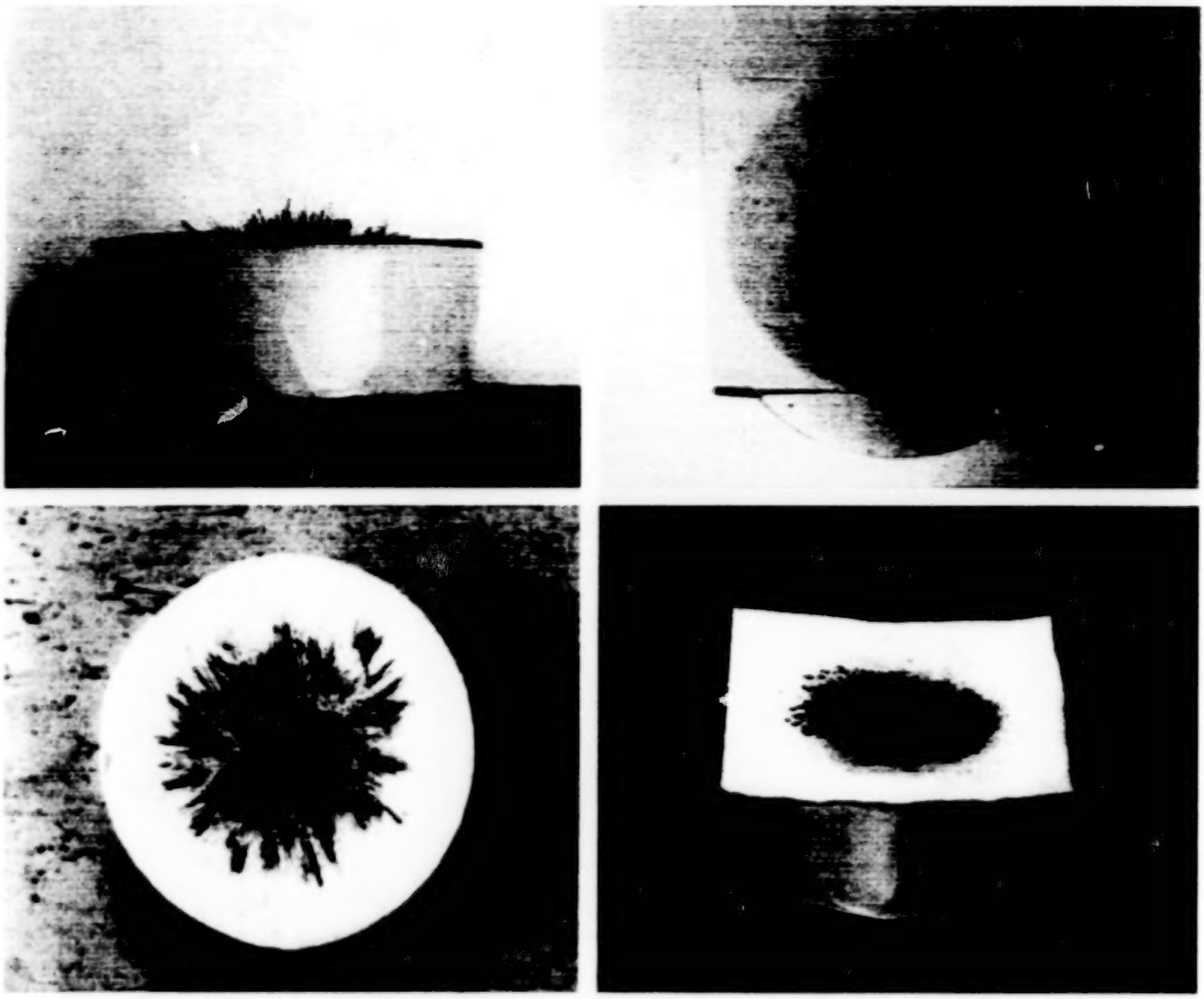

Carbon-Based Material That Contains Fe_3O_4 becomes arranged in the familiar pattern of magnetic-field lines when placed on the face of a permanent magnet. On the left are side and top views of a fibrous sample; on the right are two angle views of a powdered sample.

page 63 and "Modification of Carbon Fibers for Higher Young's Modulus" (LEW-15847) *NASA Tech Briefs*, Vol. 21, No. 4 (April 1997), page 56. In other earlier related experiments not reported in *NASA Tech Briefs*, it was found that $FeCl_3$ reacts with CF_x at temperatures between 300 and 400 °C to yield graphite intercalation compounds containing iron chloride or mixtures of iron chloride and fluoride; this finding constitutes the point of departure for the experiments reported here.

The precursor materials used in these experiments were CF_x (x ranging from 0.68 to 1.0) made, variously, from highly graphitized carbon fibers, less-graphitized carbon fibers, nongraphitized carbon fibers, and crystalline graphite powders. The experiments included exposure of $CF_{0.68}$ to $FeCl_3$ at temperatures between 280 and 420 °C to study the details of the overall general reaction $CF_x + FeCl_3 \rightarrow C$(iron halides). Between 280 and 295 °C, $FeCl_3$ quickly entered the molecular structure of $CF_{0.68}$ and broke the carbon-fluorine bonds; within 10 to 30 minutes, the $CF_{0.68}$ was completely converted to carbon made of graphite planes, between which particles of crystalline FeF_3 and noncrystalline $FeCl_2$ were located. Longer reaction times (e.g., 28 hours) or higher reaction temperatures (e.g., 420 °C) yielded materials that contained graphite, an $FeCl_3$/graphite intercalation compound, $FeCl_2 \cdot 4H_2O$, and $FeCl_2 \cdot 2H_2O$.

Materials produced in the foregoing reactions were subjected to various further heat treatments — some in air, some in nitrogen. When the heating temperatures were kept between 750 and 850 °C and the oxygen supply was kept at the optimum level, the iron halides were converted to iron oxides. When the heating temperature was increased to 900 °C, the iron oxides were reduced to iron metal. These observations led to further experiments in which, prior to the heat treatments, the materials were mixed with NiO or $NiCl_2$ in attempts to induce the formation of Fe/Ni alloys. In one successful experiment along this line, a commercial $CF_{0.7}$ powder that had been reacted with $FeCl_3$ was mixed with NiO, then the mixture was heated to a temperature of 1,200 °C for 45 minutes in quartz tubes in a nitrogen atmosphere. The product of this experiment was examined by x-ray diffraction and found to be carbon containing an Fe/Ni alloy.

This work was done by Ching-cheh Hung of **Lewis Research Center**. *Further information is contained in a TSP [see page 1].*

Inquiries concerning rights for the commercial use of this invention should be addressed to NASA Lewis Research Center, Commercial Technology Office, Attn: Tech Brief Patent Status, Mail Stop 7–3, 21000 Brookpark Road, Cleveland, Ohio 44135. Refer to LEW-16432.

Books and Reports

Evaluation of Additives to PFPEs in Boundary Lubrication

A report describes experiments on the wear-reducing performances of six additives to perfluoropolyether (PFPE)-based fluids in the boundary-lubrication regime. The additives were a phosphate, a thiophosphate, a β-diketone, a benzothiazole, an amide/thiol, and a sulfite. Each additive was dissolved, at a concentration of 1 weight percent, in a PFPE based on hexafluoropropene oxide. The resulting formulation was exposed to the boundary-lubrication regime in a four-ball vacuum tribometer at a temperature ≈23 °C, an initial Hertzian stress of 3.5 GPa, and a sliding speed of 28.8 m/s. The wear rate for each formulation was determined from the slope of wear volume as a function of sliding distance. The amide/thiol and sulfite additives were found to reduce mean wear rates by at least 80 percent. Three of the other additives were found to reduce mean wear rates by at least 55 percent. Only the benzothiazole additive exerted no wear-reducing effect. Analysis by infrared and Raman spectroscopy revealed that the severity of wear on a ball can be correlated with the amounts of fluorinated polymeric acids and of amorphous carbon on the surface of the ball, in and around the wear scar.

This work was done by William R. Jones, Jr., of **Lewis Research Center**; *Bradley A. Shogrin of Case Western Reserve University; Pilar Herrera-Fierro of Ohio Aerospace Institute; and Tzuhn-Yuan Lin and Hajimu Kawa of Exfluor Research Corp. To obtain a copy of the report, "Evaluation of Boundary-Enhancement Additives for Perfluoropolyethers," see TSPs [page 1].*

Inquiries concerning rights for the commercial use of this invention should be addressed to NASA Lewis Research Center, Commercial Technology Office, Attn: Tech Brief Patent Status, Mail Stop 7–3, 21000 Brookpark Road, Cleveland, Ohio 44135. Refer to LEW-16592.

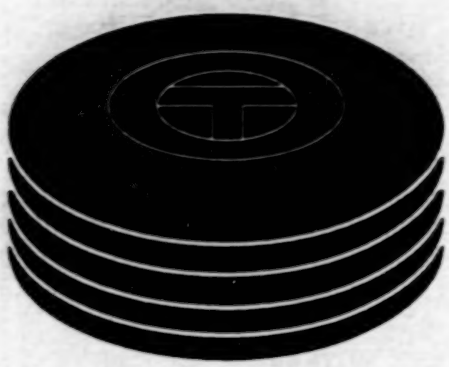

Computer Programs

Mathematics and Information Sciences

35 Program Counts Lines of Source Code

BLANK PAGE

Computer Programs

These programs may be obtained from COSMIC. Please contact

COSMIC®
Computer Services Annex
University of Georgia
Athens, GA 30602
Telephone No. (404) 542-3265.

Mathematics and Information Sciences

Program Counts Lines of Source Code

The program also provides for logging and inspection to resolve ambiguities in counts.

The Source Lines of Code Count (SLOCC) computer program counts the number of source lines of a computer code, as an aid in the management of software, documentation of code, estimation of cost, and satisfying miscellaneous code-metric needs. SLOCC accommodates the following programming languages: Ada, Pascal, C++, FORTH, Visual Basic, Z80 Assembly, and MIL-1750 Assembly. Depending on the language, SLOCC counts whichever of the following is or are applicable: source-code lines, continuations of source lines, comment lines, side comment lines (comments on the same lines with source code), end lines, blank lines, and lines of such other types as are appropriate to the target language. For some languages, this software tool provides capabilities to tabulate reference "include files," packages, functions, and so forth.

One problem often encountered in counting source-code lines is the interpretation of the count. Because of coding styles, a program could be written in such a way that some lines are counted in a manner different from what one might expect. To resolve ambiguities that arise in connection with differing interpretations and counts, SLOCC affords the capability to log all lines of code into a table, wherein each line of code is identified by type. This ability to log lines of code and inspect how they are counted can be valuable when working with computing environments that embed special directives, header information, or compiler-specific information that one might wish to count separately from source code, comments, and the like.

It is impractical to anticipate every possible variation of code, inasmuch as there are hundreds of language variants and, for each language, many environments. Given this dilemma, it is wise to inspect the table of logged code (a) until one is comfortable with the variant of code under inspection and with the SLOCC definition of "a line of code," and (b) until one agrees with this definition in one's application.

SLOCC was written in Microsoft Access Basic. SLOCC requires an IBM-PC-compatible computer that runs Microsoft Access v7.0 or higher and that contains at least 16MB of random-access memory. SLOCC has been implemented successfully under Windows 95 and Windows NT 4.0. The standard distribution medium is one 3.5-in. (8.89-cm), 1.44-MB MS-DOS-format diskette. An electronic copy of the documentation in Microsoft Word v7 format is included on the distribution medium. Sample input files are also included. SLOCC was released to COSMIC in 1997.

This program was written by Michael Neighbors of Sverdrup Technology, Inc., for **Marshall Space Flight Center**. *No further documentation is available.*
MFS-31225

BLANK PAGE

Mechanics

Hardware, Techniques, and Processes

39 Deployable and Restowable Protective Dome
40 Probes for Measuring Pressures in Flowing Gases
41 Electromagnetic Smart Washer for Detecting Bolthole Cracking
41 Bidirectional Operating Actuator (BOA)
42 Deflection of Circular Membrane Under Differential Pressure

BLANK PAGE

Deployable and Restowable Protective Dome

The design could be adapted to tents and portable sheds.

NASA's Jet Propulsion Laboratory, Pasadena, California

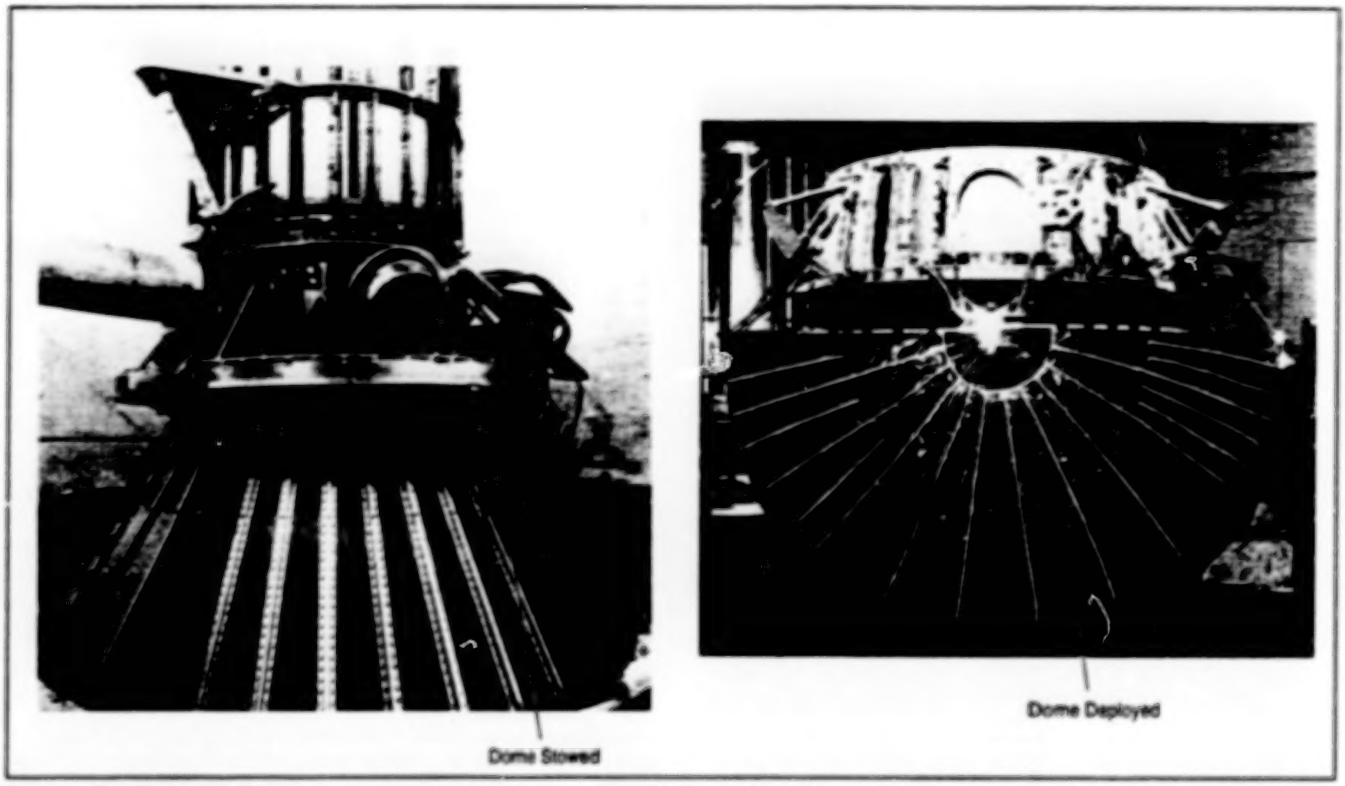

Figure 1. The **Protective Dome** can be stowed or deployed, as needed. These views show a prototype deployed in one test setup and the final product stowed for a spacecraft test.

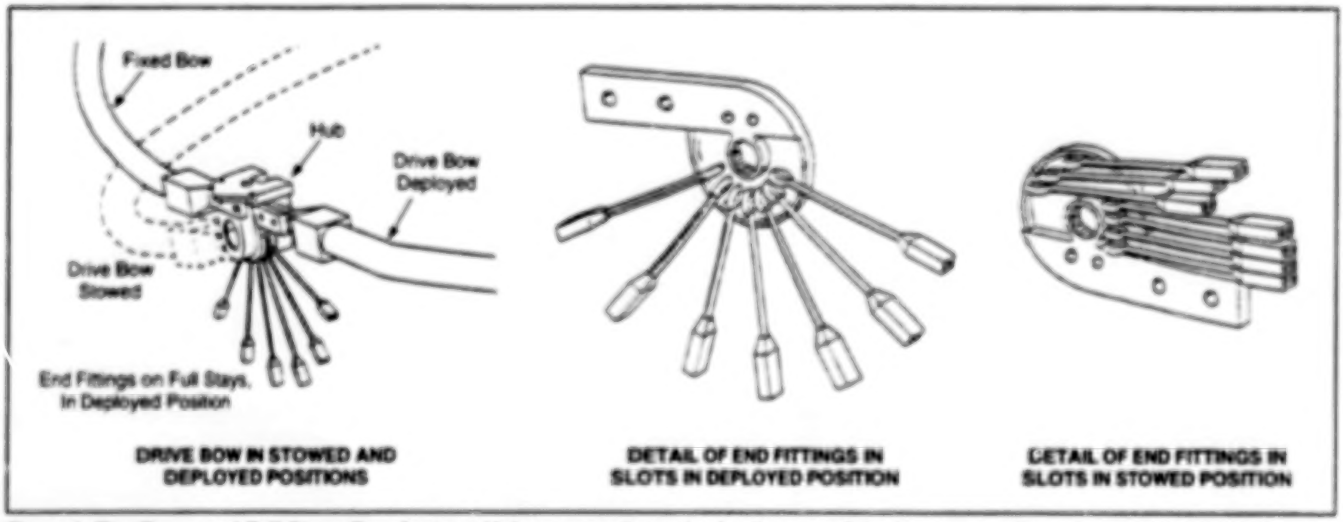
Fixed Bow
Hub
Drive Bow Deployed
Drive Bow Stowed
End Fittings on Full Stays, In Deployed Position
DRIVE BOW IN STOWED AND DEPLOYED POSITIONS
DETAIL OF END FITTINGS IN SLOTS IN DEPLOYED POSITION
DETAIL OF END FITTINGS IN SLOTS IN STOWED POSITION

Figure 2. The **Bows and Full Stays Terminate at Hubs** at opposite ends of a diameter of the hemisphere. One of the hubs is shown here in simplified form, without the drive or idler mechanism described in the text.

A deployable and restowable dome made of flexible material with semirigid reinforcements has been developed to protect the main engines of the Cassini spacecraft against impacts by micrometeoroids during the long cruise to Saturn. The design of the dome could readily be adapted to terrestrial applications in advanced, easily erectable temporary structures like tents and portable sheds.

In its appearance and basic mechanical function, the dome bears some resemblance to covers on some vintage baby carriages and cloth rooftops on convertible automobiles (see Figure 1). When fully deployed, the dome is a hemisphere approximately 2.1 m in diameter; when fully stowed, it becomes a crescent wedge less than 15 cm thick. The flexible dome material is sewn together from gore-shaped pieces with accordionlike pleats to obtain the hemispherical shape. The dome shape is supported by graphite/epoxy semicircular hoops called stays, sewn into pockets within the material. In the original Cassini spacecraft application, the flexible material

is an advanced, multilayer, thermally insulating blanket that is made electrically conductive to prevent the accumulation of static electric charge. Other, less-advanced flexible materials could likely be used in terrestrial applications like tents and sheds.

Two semicircular bows made of aluminum tubing, forming a circle on the dome at the "equator," meet at two hubs that allow them to pivot (see Figure 2). The ends of eight of the stays meet at the hub and slide in grooves, while other stays sewn into the material only support the shape of the dome. The flat shape of the stay end fittings allow the dome shape to collapse to a compact stowed position. The lollipop-shaped fittings on the ends of the stays slide freely in the slots in the hubs, with sufficient slack to allow for folding of the flexible material during stowage. One of the bows is fixed; the other is driven in rotation about the diameter to produce motion needed for deployment or stowage (see Figure 2). The drive mechanism, located at one hub, is nonbackdriveable and redundant; it includes two independent, electronically commutated dc brushless motors and two paths of 20:1 spur-gear and 605:1 harmonic output gears. In the other hub, the driven bow is retained by an idler mechanism that includes gears to transfer the rotary motion of the driven bow to a potentiometer for measurement of the angle of deployment. The rotation of the driven bow is limited by adjustable stops. A miniature lever-actuated switch at each stop provides an electrical indication that the driven bow has reached the stop.

This work was done by Donald Sevilla, Lori Shiraishi, and Randal Foehner of Caltech for **NASA's Jet Propulsion Laboratory**. *Further information is contained in a TSP [see page 1].*

NPO-20156

Probes for Measuring Pressures in Flowing Gases

Transient pressure is sensed in situ; steady pressure is coupled pneumatically to external sensors.

Lewis Research Center, Cleveland, Ohio

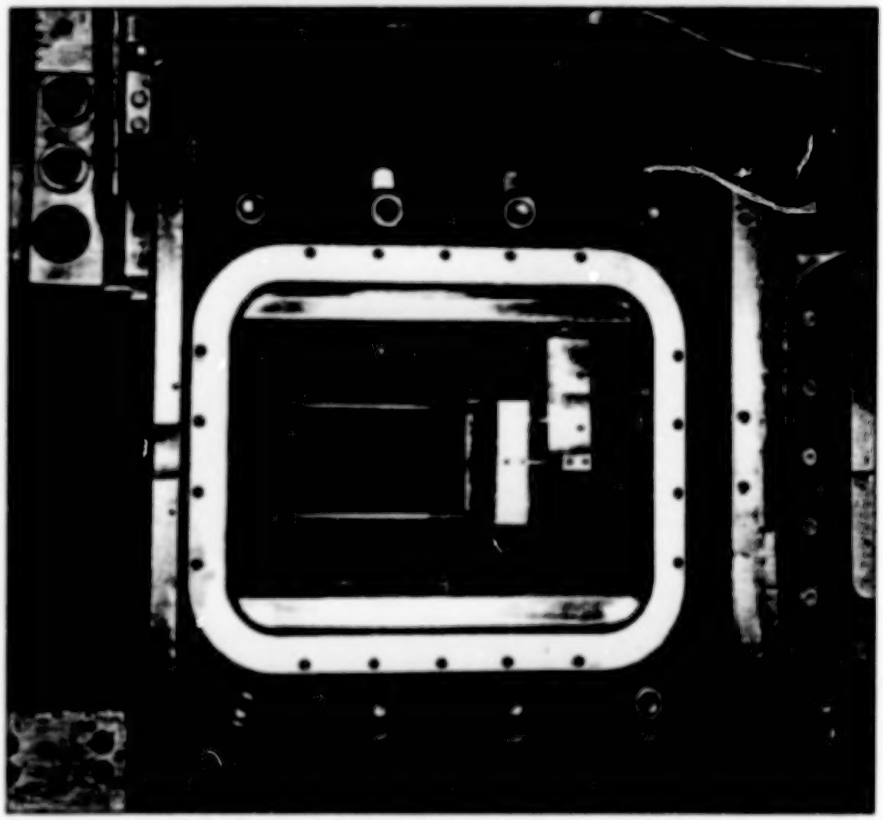

Two Prototypes of the Pressure Probes described in the text are installed in a supersonic wind tunnel.

Improved pressure probes have been designed to give nearly instantaneous readings of the time-varying local static pressure in flowing gases. The probes have been installed in a wind tunnel (see figure). Probes of this type could also be particularly useful as pressure-sensing instruments to help characterize the instantaneous airflow fields about aircraft; the outputs of these and other instruments could be used, for example, as inputs to advanced digital flight-control systems. These probes could also be used to measure local time-varying pressures in natural-gas pipelines.

The probe design is modular, featuring a variety of interchangeable tips with different shapes for different flow conditions; a cone-cylinder tip is optimized for supersonic flow, whereas a sphere/cylinder tip is optimized for subsonic flow. Each probe tip contains eight radial holes that intersect an internal pneumatic passage, part of which serves as a pressure-measurement plenum. The external shape and the configuration of the passages is designed so that the pressure in the plenum equals the local static pressure of the flow field in which the flow is immersed.

A dynamic-pressure transducer located in the plenum senses the rapidly varying component of static pressure; this transducer is connected to external high-speed electronic circuitry that samples the transducer output. The probe tip is mounted on a stem, which is hollow; the stem contains both (1) wires for connection to the electronic circuitry and (2) a passage that serves as a conventional pneumatic connection between the plenum and an external transducer that measures the slowly varying component of static pressure.

In tests, prototypes of these probes were found to respond to both transient and steady pressures, as intended. In supersonic-flow tests, the probes measured free-stream static pressures correctly at mach 1.6., 2.0, and 2.5. In the worst case encountered in the tests, the root-mean-square pressure measured by the tip transducer and the time-averaged pressure measured by the pneumatically coupled external transducer differed by no more than 0.02 psi (140 Pa). Transient testing of the prototype probe configuration indicates a dynamic static-pressure-measurement capability in excess of 800 measurements per second (800 Hz).

This work was done by A. Robert Porro and Michael E. Ernst of **Lewis Research Center**. *Further information is contained in a TSP [see page 1].*

Inquiries concerning rights for the commercial use of this invention should be addressed to NASA Lewis Research Center, Commercial Technology Office, Attn: Tech Brief Patent Status, Mail Stop 7–3, 21000 Brookpark Road, Cleveland, Ohio 44135. Refer to LEW-16348.

Electromagnetic Smart Washer for Detecting Bolthole Cracking

New device allows engineers to detect the onset and progress of bolthole cracks without removing the bolt.

Marshall Space Flight Center, Alabama

Engineers have designed a new device, called the Smart Washer, that can electromagnetically detect bolthole cracks in metal structures. The device is a metal washer that contains a wire coil embedded onto the bottom surface of the washer. An alternating current drives this coil and induces eddy currents around the bolthole. These eddy currents develop electromagnetic fields that interact with the driving field of the coil.

A sensor is built into the Smart Washer, enabling direct contact with the bolthole lip, which is a natural crack-formation site. The sensor is therefore ideally positioned for crack monitoring, and since the Smart Washer is a permanent part of the structure, technicians can detect bolthole cracks without removing the bolt.

Another advantage is that unlike bolts, washers are not critical structures. Since washers distribute bolt loads onto surfaces, Smart Washers can accommodate a sensor without degrading structural strength.

The Smart Washer technology has several novel features. First, unlike many sensing systems, the design allows a long cable between the local electronics of the Smart Washer and the measurement circuitry. If this cable is routed to an access port, then technicians can inspect boltholes by connecting a hand-held instrument.

Secondly, it is easy to fabricate Smart Washer sensing coils, and the measurements involve well-understood techniques that require relatively few components. The simplicity of the Smart Washer provides a robust, rugged system that can withstand field conditions.

Finally, because washers are not critical structures, designers are more willing to replace standard washers with Smart Washers, thereby adding embedded bolthole monitors to new and existing designs.

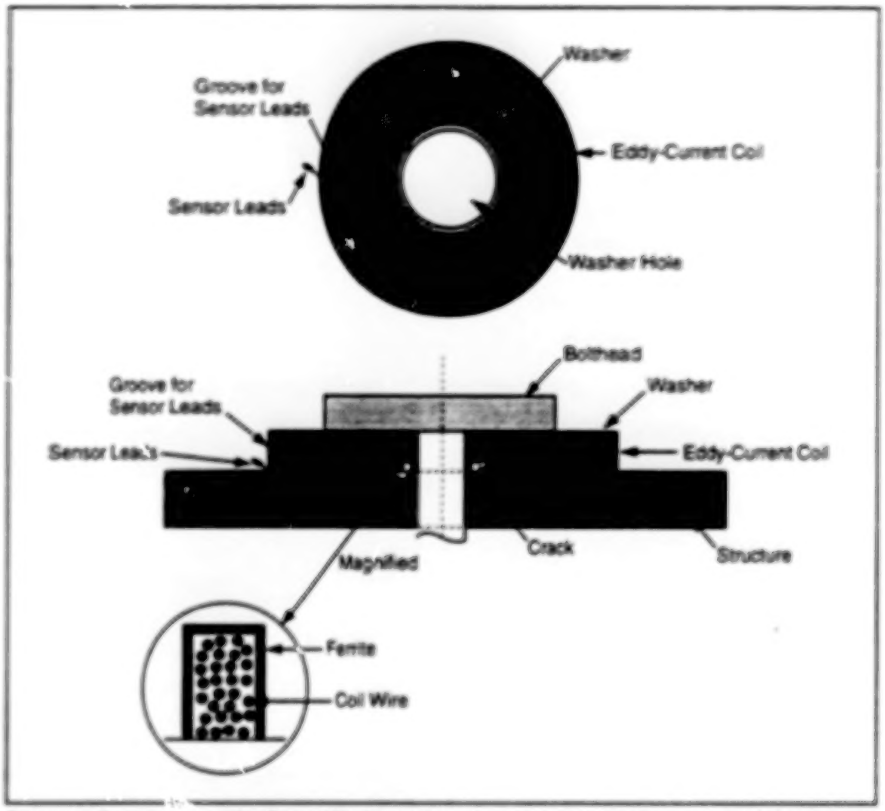

Sensors Connected to the Smart Washer detect changes in the electromagnetic fields around the bolthole, indicating bolthole cracks.

The unique capabilities of the Smart Washer have been successfully demonstrated during destructive tests. Smart Washers were mounted on 1/8-in. (3.2-mm) thick aluminum 2219-T87 coupons, where each coupon contained a 0.5-in. (13-mm) diameter drilled hole. The coupon was installed in a fatigue test machine, and the Smart Washer was fastened to the coupon with a stainless steel nut and bolt. Cyclical tensile loading induced a bolthole crack, and the Smart Washer sensor signal was recorded as the crack grew.

The Smart Washer successfully detected crack initiation and growth in conditions of dynamic loading, static loading, and unloaded conditions. In all cases, the Smart Washer could reliably detect 0.050-in. (1.27-mm) long cracks, and could track crack growth out to lengths approaching 0.200 in. (5.08 mm).

This work was done by Bruce McKee, Yuri M. Shkarlet, Atteen Khalkate, Tom Banas, Richard Ingram, and David Perkins of Innovative Dynamics, Inc., Cornell Research Park, for **Marshall Space Flight Center**. *Further information is contained in a TSP [see page 1].*

MFS-26479

Bidirectional Operating Actuator (BOA)

New device increases the stroke output of a piezoelectric transducer.

Marshall Space Flight Center, Alabama

A generic actuator has been designed to amplify the piezoelectric effect. The Bidirectional Operating Actuator (BOA) amplifies the stroke of a piezoelectric element and reorients it through a kinematic linkage.

Piezoelectric transducers are typically capable of low-strain and high-force output. The strain of a piezoelectric device is less than 0.1 percent. The force output per unit area of a piezoelectric device can be as high as 40 MPa. Piezoelectric actuators are desirable because of their direct conversion of electric potential to mechanical work. Typically, piezoelectric actuators are used in situations that require high-precision micromotion.

A longer piezoelectric stroke is often

needed. The stroke can be increased using a variety of methods. The most common method of piezoelectric stroke amplification is to use a bender element. In this case, a piezoelectric wafer is bonded to a substrate to form an "active" bimetallic strip. When a voltage is applied, the extension or contraction of the piezoelectric is converted to bending of the beam. Actuators used in this configuration are usually high-stroke, low-force devices.

Another method of increasing the stroke of a piezoelectric is to use a kinematic mechanism. The mechanisms can be simple lever arms or four-bar-type linkages. The most important factor in the design of a kinematic linkage is the use of flexure hinges — joints cut into a solid piece of material. The thin section of the joint is compliant in one direction, stiff in other directions.

The **Bidirectional Operating Actuator** is a device for increasing the stroke output of a piezoelectric transducer.

Another significant consideration with piezoelectric transducers is the type of load on the material. Since piezoelectric is a ceramic material, it is not able to withstand large tensile or bending loads. The best way to avoid tensile loads is to apply a preload to the transducer, which allows the piezoelectric to operate in compression only. With a preload, the piezoelectric provides extension while the preload provides the return force. Preloading insures firm mechanical mating between the piezoelectric and the surrounding mechanism.

This work was done by David V. Newton and Ephrahim Garcia, of Garman Systems Incorporated, for **Marshall Space Flight Center**. *Further information is contained in a TSP [see page 1].*

Inquiries concerning rights for the commercial use of this invention should be addressed to the Patent Counsel, Marshall Space Flight Center [see page 1]. Refer to MFS-26425.

Deflection of Circular Membrane Under Differential Pressure

Equations have been derived for a situation not represented in prior texts.

Goddard Space Flight Center, Greenbelt, Maryland

Equations have been derived to fill a gap in previously published standard collections of stress-and-strain formulas: These are equations for deflection of a thin circular membrane that is clamped rigidly around its periphery and subjected to differential pressure. Related equations were described in "Deflection and Stress in Preloaded Square Membrane," (GSC-13367, Vol. 15, No. 9 (September 1991), page 96 and "Deflection and Stress in Preloaded Rectangular Membrane," (GSC-13561), Vol. 18, No. 3 (March 1994), page 100.

As in the cases of the square and rectangular membranes, the derivation of the equations for the circular membrane follows a strain-energy/virtual deflection approach, which is common in stress-and-strain problems of this kind. The displacements of the membrane under load are initially assumed to be of the form

$$w = w_0\left[1-\left(\frac{r}{a}\right)^2\right]^2 \qquad (1)$$

and

$$u = r(a-r)(c_1 + c_2 r) \qquad (2)$$

where r is the radial coordinate, a is the radius of the clamping edge, w is the transverse displacement (that is, the deflection perpendicular to the nominal membrane plane) at radius r, w_0 is the maximum transverse displacement, u is the radial displacement at radius r, and c_1 and c_2 are constants.

The radial and transverse strains are given, respectively, by

$$\varepsilon_r = \frac{du}{dr} + \frac{1}{2}\left(\frac{dw}{dr}\right)^2 \qquad (3)$$

and

$$\varepsilon_t = \frac{u}{r} \qquad (4)$$

The strain energy associated with stretching of the membrane is given by

$$V = \frac{\pi E h}{1-\nu^2}\int_0^a (\varepsilon_r^2 + \varepsilon_t^2 + 2\nu\varepsilon_r\varepsilon_t)rdr \qquad (5)$$

where E is Young's modulus, h is the thickness of the membrane, and ν is Poisson's ratio.

To calculate the deflection of the membrane, one must solve the foregoing equations to find c_1, c_2, and w_0. First, one substitutes the right sides of equations (1) through (4) for the corresponding terms in equation (5). Using the resulting form of equation (5), one finds c_1 and c_2 by imposing the requirements that

$$\frac{\partial V}{\partial c_1} = 0 \qquad (6)$$

and

$$\frac{\partial V}{\partial c_2} = 0 \qquad (7)$$

Next, one imposes the requirement that the change in work done by the differential pressure acting through a virtual displacement equals the change in strain energy associated with the virtual displacement. If the virtual displacement is chosen to be $\delta w \propto \delta w_0$, then this requirement is expressed by the equation

$$\frac{\partial V}{\partial w_0}\delta w_0 = 2\pi q \delta w_0 \int_0^a \left[1-\left(\frac{r}{a}\right)^2\right]^2 rdr \qquad (8)$$

where q is the differential pressure on the membrane. The solution for the maximum displacement is

$$w_0 = \alpha a^3\sqrt{\frac{qa}{Eh}} \qquad (9)$$

where

$$\alpha = \sqrt[3]{\frac{6615(\nu^2-1)}{2(2791\nu^2 - 4250\nu - 7505)}} \qquad (10)$$

This work was done by Alfonso Hermida of **Goddard Space Flight Center**. *Further information is contained in a TSP [see page 1].*

GSC-13783

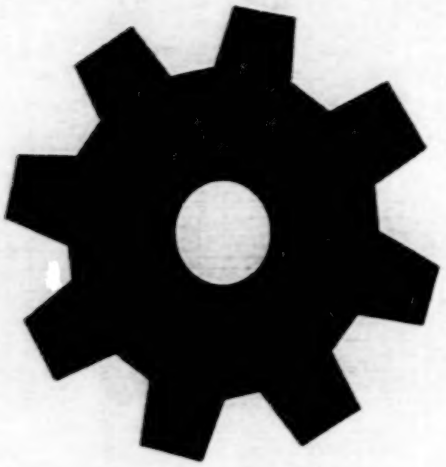

Machinery

Hardware, Techniques, and Processes

45 Electromagnetic Shaker for Flight Flutter Testing

Books and Reports

46 Micromachined Monopropellant Thrusters

BLANK PAGE

Electromagnetic Shaker for Flight Flutter Testing

Precise forcing functions can be applied for studying vibrational responses.

Dryden Flight Research Center, Edwards, California

An electromagnetic shaker based on a linear induction motor has been developed for use in flight flutter testing of aircraft. The shaker is a wing-tip-mounted unit capable of delivering root-mean-square forces as large as 140 lb (623 N) at frequencies from 10 to 60 Hz.

Advanced flight flutter testing methods that are undergoing development show promise for significantly improving the process of expansion of the flight envelope. However, these methods will require airborne equipment that can rapidly, repeatedly, and vigorously excite all of the critical vibrational resonances of an aircraft with precise, carefully crafted forcing functions, the time dependencies of which can be measured. These capabilities are well beyond those of previously developed shakers.

During the development of the present electromagnetic shaker, a linear induction motor (LIM) was combined with a field-oriented (vector) controller that enables the use of the LIM as a servo. The LIM can therefore be made to track an analog signal that represents the desired force as a function of time. As the LIM produces the commanded force, it accelerates and decelerates the mass of the moving portion of the LIM. The resulting reaction force on the nominally stationary portion (that is, the portion attached to a wing-tip accessory rail) is delivered to the wing. The field-oriented controller utilizes feedback from a position sensor and from phase current sensors, in order to control the force produced by the LIM.

A requirement for high force, plus tight constraints on weight and size necessitated a novel LIM design. In particular, as shown in the "disassembled" view in the figure, the LIM features two end primary windings, two secondary "ladder" conductors (each double-sided), and a middle double-sided primary winding in a multiple-airgap arrangement. The magnetic flux that emerges from an end primary winding must pass through the two secondary conductors, the middle double-sided primary winding, and the four airgaps before reaching the other end primary winding. Consequently, only the end primary windings must be provided with iron return paths, so that the shaker can be made very compact. In addition, designing the secondary conductors to be stationary and the primary windings to move enables

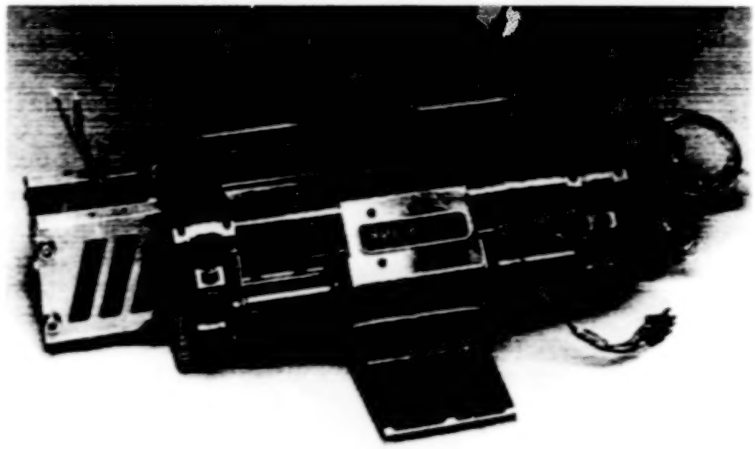

LIM ASSEMBLED

LIM DISASSEMBLED

This **Linear Induction Motor (LIM)** is designed to satisfy a requirement for high force, plus tight constraints on weight and size.

limitation of the stationary portion of the mass of the shaker to 10.5 lb (4.8 kg).

In tests, the force that the LIM can apply was found to be limited by heating. For example, if heating were not a consideration, then the LIM could produce a force in excess of 1,000 lb (4.4 kN) at electrical breakdown while operating at a magnetic field near saturation, with ohmic losses of 10 kW. On the other hand, the LIM can produce a force of 200 lb (0.9 kN) at a more reasonable level of losses (1.0 kW) at lower fields. The foregoing results imply that at low duty cycles, one can achieve forces much greater than those achievable in continuous operation. Tests also demonstrated the ability of the shaker to follow sinusoidal force commands at frequencies up to 90 Hz.

The test results indicate the feasibility of using this and other LIM-based reaction-mass actuators for both vibration-cancellation and shaker applications. The long stroke of the LIM is particularly advantageous in that it enables the LIM to generate large forces at frequencies down to <10 Hz. It might even be possible to use actuators like the present

one to replace pneumatically powered hammers in some applications.

This work was done by Fred Flynn, Ron Ghofrani, Jim Goldie, Kevin Leary, John Swenbeck, Dick Hockney, Scott Makseyn, Steve Armstrong, Gita Rao, Geoff Lansberry, Dick Satter, and Cynthia Paine of SatCon Technology Corp. under a NASA SBIR contract and Leonard Voelker of **Dryden Flight Research Center**. *Further information is contained in a TSP [see page 1].*

In accordance with Public Law 96-517, the contractor has elected to retain title to this invention. Inquiries concerning rights for its commercial use should be addressed to

SatCon Technology Corporation
161 First Street
Cambridge, MA 02142-1221
(617) 349-0821

Refer to DRC-98-04, volume and number of this NASA Tech Briefs *issue, and the page number.*

Books and Reports

Micromachined Monopropellant Thrusters

A report proposes monopropellant microthrusters for a new generation of miniature spacecraft with mission lifetimes stretching into years. These thrusters would include micromachined nozzle/chamber assemblies containing microvalves, designed according to emerging concepts of microelectromechanical systems (MEMS). Like some previously designed monopropellant thrusters, these thrusters would generate expanding gases and thereby generate thrust through catalytic dissociation of liquid hydrazine; however, these thrusters would be considerably smaller. Moreover, instead of putting catalytic pellets in chambers according to the previous designs, one would roughen the inner walls of the chambers and coat them with iridium or some other suitable catalyst. The micromachined thruster assemblies would be enclosed within aerogel bodies for thermal insulation. Each thruster would be heated with a small amount of power (< 1 W) to promote vaporization. Flow geometries and the characteristic times of residence and dissociation of hydrazine would be optimized.

This work was done by Philip Moynihan and Carl Guernsey of Caltech for **NASA's Jet Propulsion Laboratory**. *To obtain a copy of the report, "Monopropellant Hydrazine Microthruster," see TSPs [page 1].*

NPO-20159

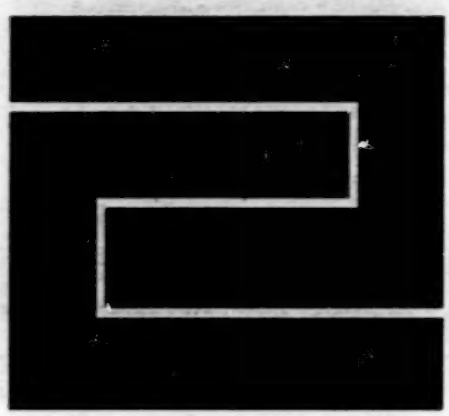

Fabrication Technology

Hardware, Techniques, and Processes

49 Magnetron Plasma Etching of SiC for Microfabrication

50 Extracting Misalignments of Layers in Microfabricated Devices

BLANK PAGE

Magnetron Plasma Etching of SiC for Microfabrication

Etch rates are high, and etched surfaces are remarkably smooth.

Lewis Research Center, Cleveland, Ohio

Magnetron plasma etching has been found to be a promising technique for micromachining of single-crystal silicon carbide to fabricate microscopic structures comprising integrated mechanical, electronic, and/or optical devices. Silicon carbide offers several advantages over silicon for the development of future devices: In comparison with silicon, silicon carbide is harder and stiffer, is less chemically reactive, and has greater thermal conductivity; moreover, silicon-carbide-based electronic devices can operate at temperatures higher than silicon-based electronic devices can withstand. Etching techniques for micromachining of silicon are well known, but the lesser chemical reactivity of silicon carbide makes it necessary to devise alternative etching techniques.

In research that preceded the development of the present magnetron-plasma-etching technique, it had been shown that single-crystal 6H-SiC could be etched at high rates to very smooth final surfaces in an electron-cyclotron-resonance (ECR) plasma reactor, using a mixture of CF_4 and O_2 gases. An ECR reactor provides a high-density plasma at a low pressure, which facilitates the formation and removal of volatile reaction products. However, the sample to be etched is remote from the main body of the plasma.

In the present magnetron-plasma-etching technique as in the ECR etching technique, a magnetic field is used to increase the density of the plasma. Unlike in ECR etching, the main body of the plasma is confined in proximity to the sample. Such confinement results in a high concentration of reactive chemical species together with a high flux of bombarding ions at the sample, making it possible to achieve rapid etching.

Magnetron plasma etching of SiC was demonstrated in preliminary experiments in a vacuum chamber, using a magnetron sputter gun as a cathode. For each experiment, a sample of 6H-SiC n-doped to a concentration $\approx 6 \times 10^{17}$ cm^{-3} was placed on a silicon target. The (0001) face of the sample was masked with a SiC fragment. A radio-frequency (RF) power supply was used, and the target was allowed to self-bias. CHF_3 and O_2 were fed into the chamber at rates fixed by mass-flow controllers. The pressure in the chamber was regulated by throttling the flow to the vacuum pump.

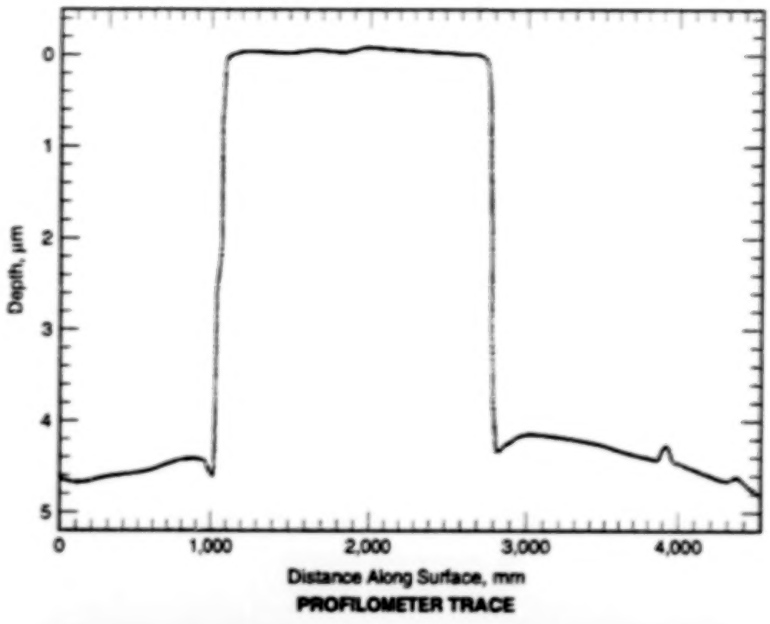

PROFILOMETER TRACE

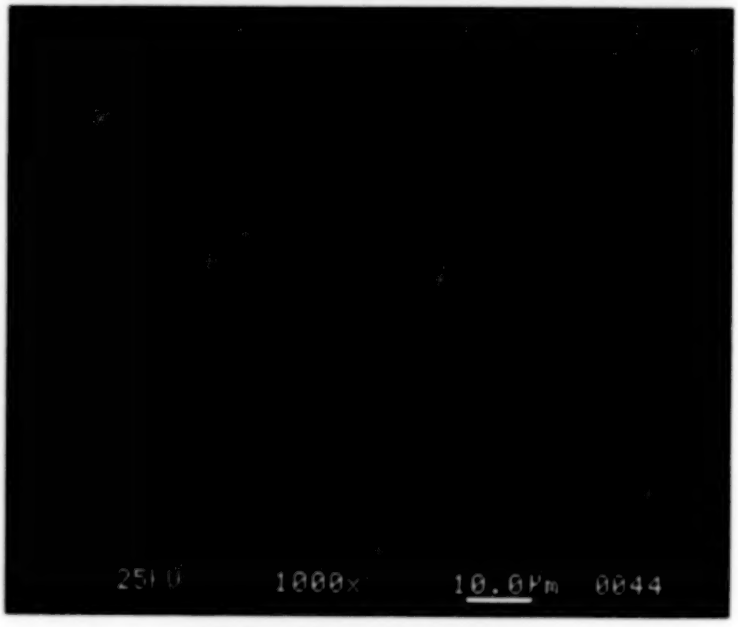

SCANNING ELECTRON MICROGRAPH

The Profilometer Trace was made after a 7-minute etch of 6H-SiC in 0.6 CHF_3 + 0.4 O_2 at a total pressure of 20 mtorr, at an RF power of 250 W. The scanning electron micrograph shows an edge of the etched region.

The duration of each etch was 7 minutes. At an RF power of 250 W, a maximum etch depth of 4.5 μm (see figure) was achieved with a gas mixture of 0.6 CHF_3 + 0.4 O_2 at a total pressure of 20 mtorr (about 2.7 Pa). This depth corresponds to an etch rate of about 640 nm per minute, which is a relatively high rate, significantly higher than that which has been achieved using an ECR plasma. The etched surface was found to have a root-mean-square surface roughness of only 20 Å. The reaction of aluminum and fluorine yields a nonvolatile product, which makes aluminum suitable for use as a mask material in order to provide selective

etching in fluorine-based plasmas. At the RF power of 250 W, aluminum films were etched at a high rate. At an RF power of 50 W, silicon carbide was etched at a rate of 170 nm per minute, while aluminum was etched at 1/12 of that rate.

This work was done by Glenn Beheim of **Lewis Research Center** *and Carl Salupo of Cortez III Service Corp. Further information is contained in a TSP [see page 1].*

Inquiries concerning rights for the commercial use of this invention should be addressed to NASA Lewis Research Center, Commercial Technology Office, Attn: Tech Brief Patent Status, Mail Stop 7–3, 21000 Brookpark Road, Cleveland, Ohio 44135. Refer to LEW-16563.

Extracting Misalignments of Layers in Microfabricated Devices

Offsets are computed from correlations between digitized images of test lines.

NASA's Jet Propulsion Laboratory, Pasadena, California

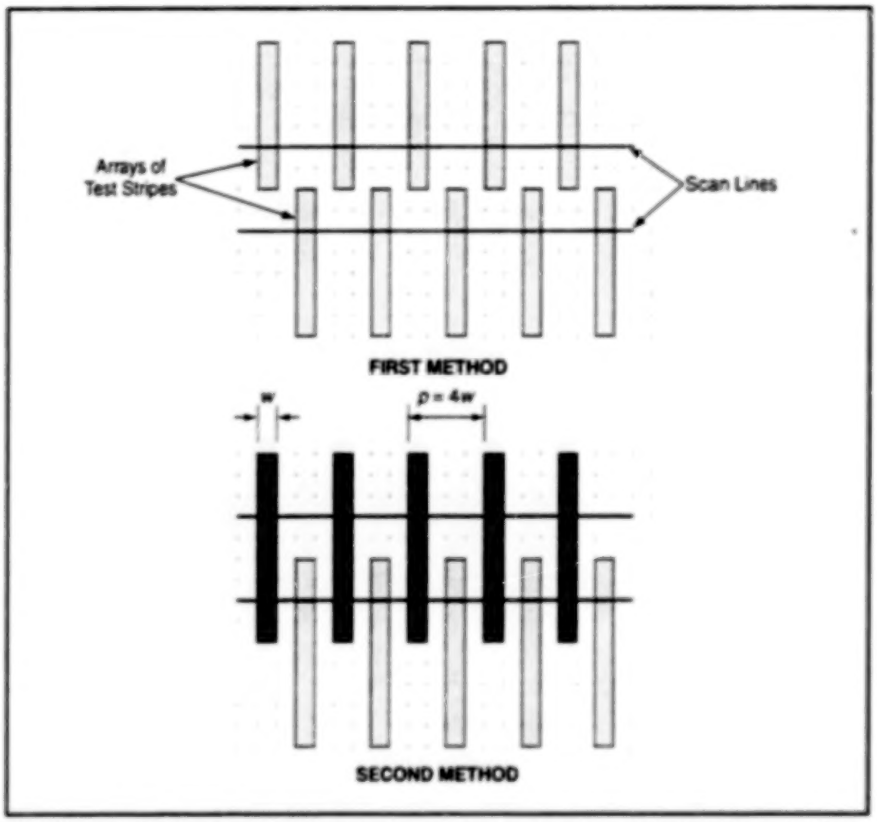

Two Arrays of Stripes are built into two layers that are to be inspected for alignment. The two different arrangements of arrays and scan lines are associated with somewhat different computational procedures for extracting misalignment distances from correlations.

Two closely related methods of optical inspection and computation yield data on misalignments between critical features in different layers of microfabricated devices. Examples of such devices containing features in different layers that are required to be aligned with each other include (1) magnetic-memory devices containing magnetic and nonmagnetic metal lines and grooves in garnet substrates, (2) integrated electronic circuits containing variously patterned metal, semiconductor, and dielectric materials, and (3) micromechanical devices. Before the development of the present methods, misalignments were determined in manual/visual procedures, in which technicians took readings from vernier or wedge test structures.

The present methods also involve the use of test structures, but most of the work of taking the readings and processing the data is automated. The test structures comprise arrays of parallel stripes of width w and pitch $p = 4w$ (see figure). These arrays are fabricated as integral parts of the layers to be inspected. Nominally, in a given test structure, the arrays in two layers of interest are parallel to each other, with the long axes of the stripes perpendicular to the coordinate axis along which misalignment is to be measured (hereafter called "the axis of interest," for short).

During inspection, a video camera is focused on the device through a high-power microscope to capture an image of the arrays of stripes. The image is digitized, and the resulting data are processed on a personal computer. The processing includes three major tasks, the first of which is a "line scan," in which digitized image intensities are taken as functions of position (with a resolution of 1 pixel) along two lines that are nominally parallel to the axis of interest. The second major task is to compute correlations between the line scans. The third major task is to determine the misalignment distance from the locations of the peaks of the correlation function.

The practices described thus far in general terms are common to both methods. The methods differ in the locations of test structures and line scans and in the associated details of computing the misalignments from the line-scan data. In the first method, the test structures are placed near each other (but not overlapping), and separate line scans are taken through the two structures. This method is valid only when deviation of the scan line from orthogonality to the test stripes is so small that any apparent shift caused by this deviation is a small fraction of a pixel.

The second method is more complex but offers the advantage of eliminating the requirement of orthogonality. In this method, the two test structures are partly interdigitated, and two line scans are performed. The first line scan is taken through whichever test structure is more clearly defined in the video image. The second line scan is taken through both test structures in the overlap region. In this method, the shift associated with nonorthogonality and the misalignment between the test structures are computed from a combination of the correlation between both line scans of the first test structure and the correlation between the line scans of the two structures. In an experiment, these methods yielded data on misalignments between grooves in a garnet substrate and metal stripes (in another layer) with an error less than half of the 0.5-μm fabrication tolerance of the specimen.

This work was done by Udo Lieneweg of Caltech for **NASA's Jet Propulsion Laboratory**. *Further information is contained in a TSP [see page 1].*
NPO-20016

National Aeronautics and
Space Administration

END

02\09\99